Solar Phys
DOI 10.1007/s11207-016-0978-y

Moreton and EUV Waves Associated with an X1.0 Flare and CME Ejection

Carlos Francile[1] · Fernando M. López[2] · Hebe Cremades[3,4] · Cristina H. Mandrini[5,6] · María Luisa Luoni[5] · David M. Long[7]

Received: 11 March 2016 / Accepted: 16 August 2016

Abstract A Moreton wave was detected in active region (AR) 12017 on 29 March 2014 with very high cadence with the *H-Alpha Solar Telescope for Argentina* (HASTA) in association with an X1.0 flare (SOL2014-03-29T17:48). Several other phenomena took place in connection with this event, such as low-coronal waves and a coronal mass ejection (CME). We analyze the association between the Moreton wave and the EUV signatures observed with the *Atmospheric Imaging Assembly* onboard the *Solar Dynamics Observatory*. These

Waves in the Solar Corona: From Microphysics to Macrophysics
Guest Editors: Valery M. Nakariakov, David J. Pascoe, and Robert A. Sych

Electronic supplementary material The online version of this article (doi:10.1007/s11207-016-0978-y) contains supplementary material, which is available to authorized users.

✉ C.H. Mandrini
mandrini@iafe.uba.ar

C. Francile
cfrancile@unsj-cuim.edu.ar

F.M. López
flopez@icate-conicet.gob.ar

H. Cremades
hebe.cremades@frm.utn.edu.ar

M.L. Luoni
mluoni@iafe.uba.ar

D.M. Long
david.long@ucl.ac.uk

1 Observatorio Astronómico Félix Aguilar (OAFA), UNSJ, San Juan, Argentina

2 Instituto de Ciencias Astronómicas, de la Tierra y del Espacio (ICATE), CONICET, San Juan, Argentina

3 Facultad Regional Mendoza, Universidad Tecnológica Nacional, Mendoza, Argentina

4 Consejo Nacional de Investigaciones Científicas y Técnicas (CONICET), Mendoza, Argentina

5 Instituto de Astronomía y Física del Espacio (IAFE), CONICET-UBA, Buenos Aires, Argentina

include their low-coronal surface-imprint, and the signatures of the full wave and shock dome propagating outward in the corona. We also study their relation to the white-light CME. We perform a kinematic analysis by tracking the wavefronts in several directions. This analysis reveals a high-directional dependence of accelerations and speeds determined from data at various wavelengths. We speculate that a region of open magnetic field lines northward of our defined radiant point sets favorable conditions for the propagation of a coronal magnetohydrodynamic shock in this direction. The hypothesis that the Moreton wavefront is produced by a coronal shock-wave that pushes the chromosphere downward is supported by the high compression ratio in that region. Furthermore, we propose a 3D geometrical model to explain the observed wavefronts as the chromospheric and low-coronal traces of an expanding and outward-traveling bubble intersecting the Sun. The results of the model are in agreement with the coronal shock-wave being generated by a 3D piston that expands at the speed of the associated rising filament. The piston is attributed to the fast ejection of the filament–CME ensemble, which is also consistent with the good match between the speed profiles of the low-coronal and white-light shock waves.

Keywords Flares, waves · Coronal mass ejections, low coronal signatures · Waves, propagation · Waves, shocks

1. Introduction

Coronal mass ejections (CMEs) and flares are the most energetic events that occur in the solar atmosphere. Their effects are detectable not only close to the Sun, but also far into the interplanetary medium; they are key drivers of space-weather conditions. CMEs and flares can be observed separately or in conjunction, and they are generally associated with large active regions (ARs) with a complex magnetic field structure. The influence of flares and CMEs on the solar atmosphere includes a wide variety of phenomena, such as radio bursts, accelerated particle beams, formation of transient coronal holes, shocks, and large-scale propagating perturbations like Moreton and extreme ultraviolet (EUV) waves, among others (*e.g.* Benz, 2008; Chen, 2011; Webb and Howard, 2012).

Globally propagating waves as a byproduct of flares were first explained by Uchida (1968), Uchida, Altschuler, and Newkirk (1973). Uchida's magnetohydrodynamic (MHD) model interpreted the disturbances observed in Hα, which were discovered by Moreton (1960), Moreton and Ramsey (1960), and Athay and Moreton (1961). These so-called Moreton waves were observed in association with the most impulsive flares as arc-shaped fronts with a restricted angular span propagating with speeds of $500-1500\ \mathrm{km\,s^{-1}}$ to distances of up to 400 Mm. In Uchida's model, a coronal fast-mode MHD wave, or eventually a shock, originates within an AR, evolves as a full 3D wave-dome out to the corona, and produces enhanced Hα emission when it impacts and sweeps the chromosphere. Warmuth *et al.* (2001, 2004a, 2004b; see Warmuth, 2015 and references therein) found that Moreton perturbations slow down as they propagate, while their intensity profiles in Hα decrease and broaden as they move away from their source. In their view, and in agreement with Uchida's model, this behavior could be explained by a freely propagating fast-mode MHD shock created by a large-amplitude single pulse, which might finally decay to an ordinary fast-mode MHD wave. The analysis of numerical simulations by Vršnak *et al.* (2016) addresses the necessary

6 Facultad de Ciencias Exactas y Naturales (FCEN), UBA, Buenos Aires, Argentina

7 UCL-Mullard Space Science Laboratory, Holmbury St Mary, Dorking, Surrey RH5 6NT, UK

conditions for an eruption to cause an observable Moreton wave and a coronal shock front, with weaker eruptions producing only coronal and transition region signatures. According to their results, the perturbation evolves as a freely propagating simple wave after the initial eruption-driven phase.

Observational evidence of coronal waves in the EUV range was first reported by Moses *et al.* (1997) and Thompson *et al.* (1998) using data from the *Extreme Ultraviolet Imaging Telescope* (EIT: Delaboudinière *et al.*, 1995) onboard the *Solar and Heliospheric Observatory* (SOHO) satellite. These so-called EIT waves seen on the solar disk show slower propagating speeds than Moreton waves, about $200-400\,\mathrm{km\,s^{-1}}$, and are visible for $\approx 45-60$ min after the event that generates them. The EUV fronts propagate almost radially from an AR, with a span of up to 360°, to distances beyond one solar radius. They are usually faint and diffuse and weaken as they propagate. However, they are occasionally seen as an arc-like sharp front, in which case they are called S-waves or brow waves (Warmuth, 2015 and references therein). Evidence of large-scale wavefronts has also been observed in soft X-rays (see *e.g.* Khan and Aurass, 2002; Narukage *et al.*, 2002, 2004; Hudson *et al.*, 2003). They are observed as arc-shaped emission enhancements, are more homogeneous, and have sharper leading edges than those of EIT waves.

The discrepancy between Moreton- and EIT-wave speeds started a controversy over years about the nature of EIT waves and their role as coronal counterparts of the observable chromospheric phenomenon (see Warmuth (2015) and references therein). This discrepancy led to suggestions that the two phenomena were physically different and propagated independently. Warmuth *et al.* (2001) proposed that the mismatch in speeds might arise because Moreton waves are always seen to decelerate (see *e.g.* Warmuth *et al.*, 2004a,b; Narukage *et al.*, 2008; Muhr *et al.*, 2010; Balasubramaniam *et al.*, 2010; Warmuth, 2010; Asai *et al.*, 2012; Francile *et al.*, 2013), while the very low temporal cadence of EIT might lead to an undersampling of the early stages of the wave propagation. These authors also showed that Moreton- and EIT-wavefronts are nearly cospatial and have a similar morphology, which strongly suggests that a single physical disturbance could generate both.

A significant observational progress resulted from the next generation of EUV imagers with higher temporal cadence, such as the *Extreme Ultraviolet Imager* (EUVI: Wuelser *et al.*, 2004) onboard the two spacecraft of the *Solar-Terrestrial Relations Observatory* (STEREO: Kaiser *et al.*, 2008), the *Sun Watcher using Active Pixel System Detectors and Image Processing* (SWAP: Halain *et al.*, 2010, 2013; Seaton *et al.*, 2013) onboard the *Project for On-Board Autonomy 2* (PROBA2), and the *Atmospheric Imaging Assembly* (AIA: Lemen *et al.*, 2012) onboard the *Solar Dynamics Observatory* (SDO: Pesnell, Thompson, and Chamberlin, 2012). The data provided by these imaging instruments have helped to understand some long-standing problems about the nature of the EIT waves. EUV waves have been observed with EUVI (*e.g.* Veronig, Temmer, and Vršnak, 2008; Long *et al.*, 2011; Warmuth and Mann, 2011) and AIA (*e.g.* Long, DeLuca, and Gallagher, 2011; Liu *et al.*, 2012; Cheng *et al.*, 2012). Recently, the simultaneous existence of more than one type of EUV wave became evident from observations taken with AIA. Asai *et al.* (2012) first reported cotemporal observations of EUV and Hα Moreton waves using SDO/AIA. They identified a dome-shaped shock front expanding outward in the corona, which would produce a sharp EUV front at low coronal heights and a Moreton wave intersecting the chromosphere. They also observed a type II radio burst consistent with the shock wavefront.

Observations of shock-wave domes evolving outward in the corona as predicted by Uchida's model have previously been reported in a number of cases (*e.g.* Narukage *et al.*, 2004; Veronig *et al.*, 2010; Kozarev *et al.*, 2011; Ma *et al.*, 2011). Along these lines, 3D MHD numerical simulations performed by Selwa, Poedts, and DeVore (2012, 2013)

showed that twisted coronal magnetic loops can evolve into an EUV wave, which forms a dome-shaped structure that propagates in the corona after energy release in a flare followed by a dimming. The EUV wave propagates nearly isotropically on the disk and is able to produce the observed low-coronal and chromospheric signatures.

The aforementioned large-scale EUV perturbations have historically been named EIT waves (see the review by Warmuth, 2015). In this article, to avoid referring to a specific instrument name, we use the term EUV wave in general. Moreover, we distinguish, when needed, between their near-surface imprints in the low corona (near-surface EUV wave) and the signatures of the 3D dome seen in projection (3D-dome EUV wave).

EUV waves are often categorized into fast and slow waves (Liu *et al.*, 2010; Ma *et al.*, 2011; Chen and Wu, 2011; Liu and Ofman, 2014). Fast waves are thought to be shock waves linked to chromospheric Moreton waves and coronal soft X-ray waves (Asai *et al.*, 2012; White, Balasubramaniam, and Cliver, 2014; Cliver, 2013), while slow waves could be real waves or belong to the category of non-MHD traveling perturbations or pseudo-waves (Warmuth, 2015). Some authors have suggested a third category of EUV waves, hybrid waves, considering that in some events multiple bright fronts can be observed in conjunction, with some being true waves and others being pseudo-waves (Patsourakos and Vourlidas, 2012).

The category of pseudo-waves has been developed by several authors who proposed that EIT waves are the consequence of the magnetic field reconfiguration during a CME eruption (see *e.g.* Delannée and Aulanier, 1999). The apparent EIT wave is then the projection on the disk of an expanding CME envelope or its footpoints. Depending on the global or surrounding magnetic topology, propagating and stationary brightenings can be observed. Delannée and Aulanier (1999) (see also Delannée, 2000; Delannée *et al.*, 2008) proposed another non-wave model for EIT disturbances, arguing that the disturbances would result from Joule heating in electric-current shells during the opening of field lines in a CME ejection. Chen *et al.* (2002), Chen and Fang (2005), Chen, Fang, and Shibata (2005), Chen, Ding, and Fang (2005) suggested that a propagating density enhancement near the solar surface, which appears in numerical simulations of a rising flux rope due to the expansion of field lines, is responsible for EIT waves; while Moreton waves correspond to the faster shock front that is a consequence of the flux-rope radial acceleration. Attrill *et al.* (2007, 2009) proposed an alternative mechanism to explain EUV-wave diffuse fronts: they argued that the fronts might be generated by propagating magnetic reconnections during the expansion of CME flanks.

Another long-standing problem is related to the origin of Moreton and associated coronal EUV waves and is described by the question of what drives them: flares or CMEs. It is also unclear whether it is even possible to distinguish between these two drivers. Since CMEs and flares are able to liberate enormous amounts of energy in a short period of time, they can both be candidates to produce strong shock-waves in the corona. During Moreton events, CMEs and flares appear to originate in the same AR and occur nearly simultaneously, so that it is difficult to discern which is primarily responsible for the coronal shock wave and the chromospheric effect. The characteristics of a shock wave depend mainly on the 3D temporal piston that generates it (Vršnak and Cliver, 2008). Moreton waves exhibit the characteristics of a blast wave, as mentioned previously, *i.e.* a single shock that freely propagates and decays with time and distance. A blast wave could be generated by a 3D piston in expansion acting in a short time, as is the case of a pressure pulse caused by the flare energy deposition in the lower atmosphere. A 3D-piston driver acting for longer times and expanding in all directions, as is the case of a CME, could supply energy in a continuous way to the shock. As a consequence, the shock would evolve faster than the piston, which would generate a supersonic wave, even in the case of a subsonic driver. In this case the shock is expected to maintain the characteristic shape of the driver. There are other different types of 3D pistons, *i.e.* a rigid body or an expanding blunt driver moving through the

plasma and generating a shock cone or a hyperbole-shaped surface (called bow shock). The capability of a piston to generate a shock wave depends mostly on its size and acceleration (Temmer *et al.*, 2009), in addition to the characteristics of the coronal medium in which it propagates. In this regard, a small and impulsively accelerated driver is able to generate coronal shocks. Therefore, other phenomena are candidates for generating globally propagating coronal waves, *i.e.* eruptive filaments and small-scale ejecta (Warmuth, 2015, and references therein). Recent multidirectional observations performed with STEREO and SDO showed a direct relation between CMEs and EUV waves (see Patsourakos and Vourlidas, 2012, and references therein). The CME and the wave, initially cospatial, decouple after the initial stages of the CME evolution and the shock wave becomes a freely propagating MHD wave. This suggests that in its first steps the CME expansion acts as a temporary 3D piston that drives the shock wave. In this scenario, the CME bubble should follow the coronal wave expansion.

With the aim of contributing to the understanding of EUV waves, chromospheric Moreton waves, and their sources, we present a detailed analysis of the kinematics and directional characteristics of the wave event on 29 March 2014. An X1.0 class flare (SOL2014-03-29T17:48) occurred on that date in AR 12017 (N10 W32). This event was recorded by several observatories from the ground and by the *Interface Region Imaging Spectrograph* (IRIS: De Pontieu *et al.*, 2014), SDO, STEREO, the *Reuven Ramaty High Energy Solar Spectroscopic Imager* (RHESSI: Lin *et al.*, 2002), and *Hinode* (Kosugi *et al.*, 2007). GOES soft X-ray emission started to rise at around 17:35 UT and peaked at 17:48 UT. The flare was accompanied by a filament eruption, chromospheric and EUV waves, and a CME. The morphology of the flare onset and the magnetic field structure have been studied by Kleint *et al.* (2015) and Liu *et al.* (2015). The event began with an asymmetric filament eruption, its western portion arched upward at $\approx$17:35 UT and remained quasi-static for a few minutes. This was accompanied by a sustained increase in X-ray emission observed by RHESSI. After this first stage, the filament started to erupt at $\approx$17:43 UT, which led to a CME. Two hard X-ray sources appeared at $\approx$17:45 UT within the two elongated flare ribbons seen by IRIS in 1400 Å. The event was front-sided from Earth's view and back-sided when viewed from STEREO A and B spacecraft. EUV images showed a global coronal bright front that began to expand around 17:45 UT. The coronal bright front, accompanied by a coronal dimming, expanded to the north, west, and east, while Hα high-resolution images showed a Moreton wave. These wavefronts constitute the subject matter of this article.

Our article is organized as follows. In Section 2 we describe the data. Section 3 presents our qualitative analysis of the wave events at different atmospheric levels (chromosphere, low corona) and of their white-light counterpart. In Section 4 we perform a quantitative study of the shock-front properties and propose a geometrical model to explain the observed wavefronts as the chromospheric and EUV traces of an expanding and outward-traveling bubble intersecting the Sun. Finally, in Section 5 we discuss our results and conclude.

2. The Data

AIA provides full-disk images of the low corona with a pixel spatial size of 0.6″ and a temporal resolution of 12 s in multiple wavelengths. This characterizes AIA as the best instrument to date for the analysis of coronal waves in the EUV range (see the review by Liu and Ofman, 2014).

To study the coronal bright fronts on 29 March 2014, we used the AIA passbands centered on Fe IX (171 Å), Fe XII/XXIV (193 Å) and Fe XIV (211 Å), in which plasma emission at temperatures in the range of 0.5 – 2.5 MK can be detected. To allow for comparisons with

the Moreton-wave data, we also analyzed images captured with the filter centered on He II (304 Å). The He II passband detects plasma in the transition region with a characteristic temperature of $\approx 5 \times 10^4$ K. AIA images between 17:35 UT and 18:15 UT were processed using the Solar Software standard procedures and were rebinned to 2048^2 pixels to decrease memory requirements and to increase the signal-to-noise ratio. To avoid variations in the background of the images, we chose to use AIA images with exposure times longer than 0.06 s for the 171 Å, 211 Å, and 304 Å bands and 0.6 s for the passband centered on 193 Å. This selection criterion results in time differences between consecutive images of 24 s at most. The images were derotated to a pre-event time (17:30 UT) to correct for the displacement of coronal structures that is due to the differential rotation of the Sun.

To study the Moreton wave, we used high-temporal resolution Hα images obtained with the *H-Alpha Solar Telescope for Argentina* (HASTA: Bagalá *et al.*, 1999; Fernandez Borda *et al.*, 2002; Francile *et al.*, 2008). HASTA is located at the Estación de Altura U. Cesco of the Observatorio Astronómico Félix Aguilar, in El Leoncito, San Juan, Argentina. HASTA records images at the hydrogen Hα line center (656.27 nm, 0.03 nm FWHM) and in its red and blue wings (± 0.5 nm). The instrument has two operation modes: patrol mode and flare mode. In patrol mode, the camera obtains images with a cadence of 2 min. Solar activity is analyzed in real time; when an event with an intensity above a certain level is detected, the camera switches to flare mode. In this mode, HASTA can image the Sun with a five-second temporal cadence in the Hα line center. The high temporal cadence in the flare mode makes HASTA a suitable instrument to study Moreton waves; in particular during the initial propagation phase. HASTA images have 1280×1024 pixels with a spatial resolution of $\approx 2''$. In this article, we use a set of Hα line-center images acquired with a 50-millisecond exposure time between 17:41 UT and 17:53 UT, covering the whole Moreton event with a five-second temporal cadence. The images were pre-processed following a standard instrument procedure, scaled, and rotated to match AIA frames. To correct for the jitter produced by the seeing, we applied a cross-correlation technique to center AR 12017 in all images.

3. The Wave Event on 29 March 2014

In the following sections, we analyze propagating disturbances that evolve at different atmospheric levels using remote-sensing data recorded in several spectral bands. To measure and compare these dissimilar data, we defined two measurement frameworks, a surface frame and a plane-of-sky frame. The first is intended to be used with chromosphere and transition region data, *i.e.* those registered in the Hα and He II bands. The related emissions take place close to the solar surface, and in consequence should be measured over a curved surface, namely the solar sphere. The plane-of-sky frame is useful to measure emissions at low coronal heights, such as those in the AIA coronal EUV bands (*e.g.* 193 Å and 211 Å). The bulk of these emissions comes from a certain coronal height, but we used the data to delineate features propagating at different altitudes, like dome-shaped shock wavefronts, whose borderline can be considered as approximately located in the plane-of-view of the analyzed images. In consequence, we define the plane-of-sky frame, which is flat as opposed to the surface frame.

3.1. Hα and He II Wave

The Moreton-wave event on 29 March is detectable in HASTA images by applying running-difference techniques. It appears as a diffuse arc-shaped front propagating to the north of AR 12017 and evolving after the flare impulsive phase. Similar features can be detected in

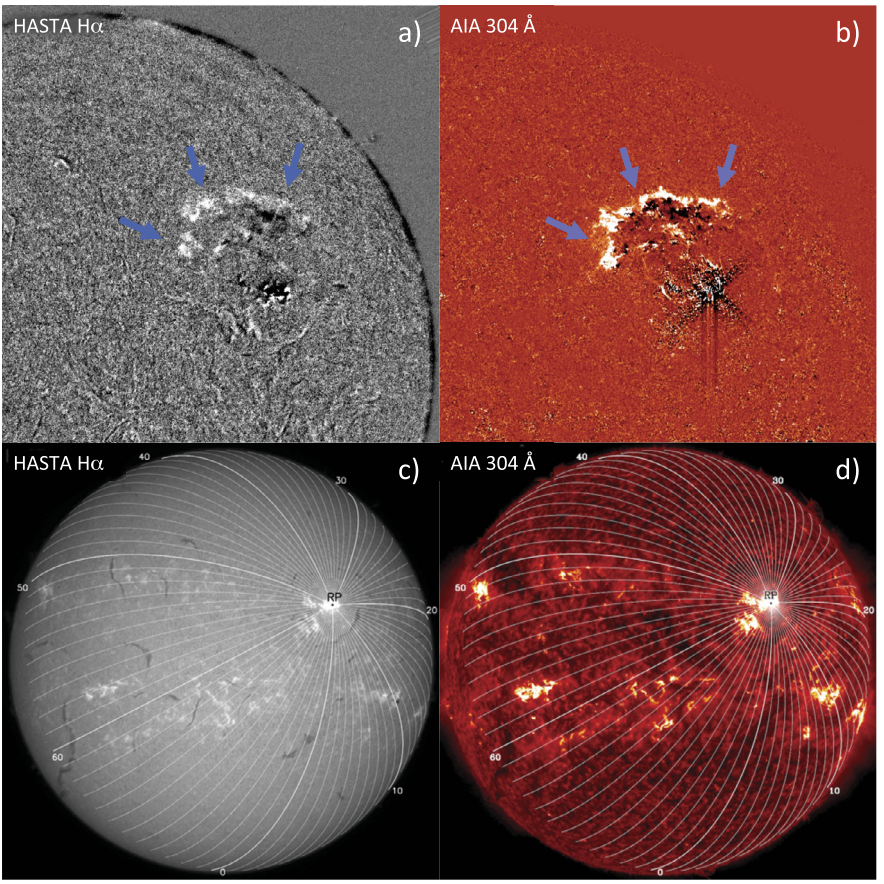

Figure 1 (a) A view of the Moreton wave in a running-difference Hα image at 17:49:42 UT (see Movie-Halpha). (b) Similar to panel a in He II at 17:49:31 UT (see Movie-304). The light blue arrows in both panels point to the propagating perturbation. (c) Great circles traced on an image recorded at the center of the Hα line at 17:43:53 UT. (d) Similar to panel c in the He II band at 17:38:07 UT. The circles are traced on the surface of the solar sphere, *i.e.* with a radius of 1 $R_{\odot}$, and depart from the radiant point defined as the site where the flare is strongest (coordinates N10.3 W32.8). The 72 sectors separated by 5° each are arbitrarily numbered in a counterclockwise order, beginning from the sector that is centered on the solar South Pole. Some of the sectors have been numbered. The tracing corresponds to an angular span of $\alpha = 100°$ from the radiant point. The field of view in panels c and d is 2.08×2.08 $R_{\odot}$.

the AIA He II (304 Å) band. A running-difference full-disk image movie built from Hα data is attached to this article (see Movie-Halpha), as well as a running-difference subfield image movie in the He II (304 Å) band (see Movie-304).

We determined the kinematic characteristics of the Moreton wave using the intensity profiles technique (Vršnak *et al.*, 2002). The intensity profiles $[\delta(\mathbf{r}_i, t_j)]$ are obtained from the running-difference image corresponding to time t_j along paths $\mathbf{r}_i$ traced on the solar disk (surface frame). The paths $\mathbf{r}_i$ are the plane projection of great circles of the solar sphere passing through a radiant point (RP, see Figure 1c and 1d). We approximated the actual site of origin of the wave event, *i.e.* the RP, as the centroid of the most intense flare kernel in the AR that corresponds to 514.2″ in the east–west and 263.4″ in the north–south directions in the heliocentric-Cartesian coordinate system and N10.3 W32.8 in the heliographic system.

The intensity profiles $[\delta(\mathbf{r}_i, t_j)]$ were discretized in angular steps, starting from the RP, along the corresponding great circle with a resolution of 0.1°. Each discrete value is computed by averaging the intensity values laterally over an angular sector of 5° centered on the RP. In this way, the solar surface distance from the RP to a certain point P of the path $\mathbf{r}_i$ can be computed as $d_c = \alpha \times 1R_\odot$, where α is the angle subtended between the two radial vectors formed by the pairs of points (O, RP) and (O, P) in 3D, where O is the center of the solar sphere.

To investigate the angular dependence of the evolution of the wave event, we applied a stack plot procedure (Liu *et al.*, 2010; Li *et al.*, 2012). In this way, distance–time (DT) maps were built by stacking in columns the intensity profiles $[\delta(\mathbf{r}_i, t_j)]$ corresponding to a specific path $\mathbf{r}_i$ over the full time-span of the wave event. These columns were expanded for the time span between the corresponding image of the set and the next one, therefore the DT-maps abscissae are in seconds. The DT-map ordinates are the surface distance $[d_c]$ measured from the RP.

We covered the 360° around the RP with 72 sectors of 5° each, thus obtaining 72 DT maps in correspondence with the 72 paths $[\mathbf{r}_i]$, numbered counterclockwise starting from a great circle passing through the solar South Pole. Figure 1 shows the 72 sectors superimposed to Hα (panel c) and He II (panel d) images. The reference sector 0 is centered on the solar South Pole and starts at the great circle denoted with a thick white line.

The results of this procedure for sectors 31 to 46 can be observed in Figure 2. The Moreton wave is visible in Hα DT-maps (Figure 2a) as an oblique bright trace for all the displayed sectors. The slope of these traces indicates the speed of the Moreton wave in the corresponding sector. The region where the traces are brighter, *i.e.* between sectors 35 to 46, shows an initial brief lapse of deceleration, after which the speed of the Moreton wave is almost constant. Sectors 36 to 39 show regions with an apparent overlap of two traces very close in time (see the insets in the corresponding sector panels). He II DT-maps (Figure 2b) show similar oblique traces. The traces are not continuous and have the appearance of a succession of parcels with fluctuating intensity. No overlap of the traces can be discerned, in contrast to the Hα DT-maps. The vertical stripes in the background correspond to changes in the exposure time of AIA during the recording of the flare peak-intensity.

We obtained light curves of the whole flaring region, shown in Figure 3 for Hα (panel a) and He II (panel b). To compare these curves, which have a similiar temporal evolution but a different intensity scale, we divided them by their maximum intensity value, *i.e.* we normalized them. From these curves we derived a flare onset time as the peak of the derivative of the light curves. The derivative was computed using a standard quadratic three-point Lagrangian interpolation. The values obtained are $t = 17{:}45{:}15.82$ UT for Hα and $t = 17{:}45{:}20.57$ UT for He II. We chose the value obtained from Hα as the reference flare onset time $[t_{on} = 17{:}45{:}16]$ because of the higher temporal cadence of the HASTA telescope in flare mode.

3.2. EUV Waves

Several propagating features with dissimilar characteristics are visible in AIA images at 171 Å, 193 Å, and 211 Å, some of which are displayed in panels a, b, and c of Figure 4. Movies of running-difference images in these bands accompany this article (see Movie-171, Movie-193, and Movie-211). Figure 4a shows a running-difference 171 Å image at $t = 17{:}50{:}23$ UT superimposed on magnetic field contours of a *Helioseismic Magnetic Imager* (HMI: Scherrer *et al.*, 2012) magnetogram. The contours show the complex magnetic structure of AR 12017, while the large-scale loops to the east indicate its connectivity to scattered negative-polarities belonging to a large bipolar region. The light blue arrows in

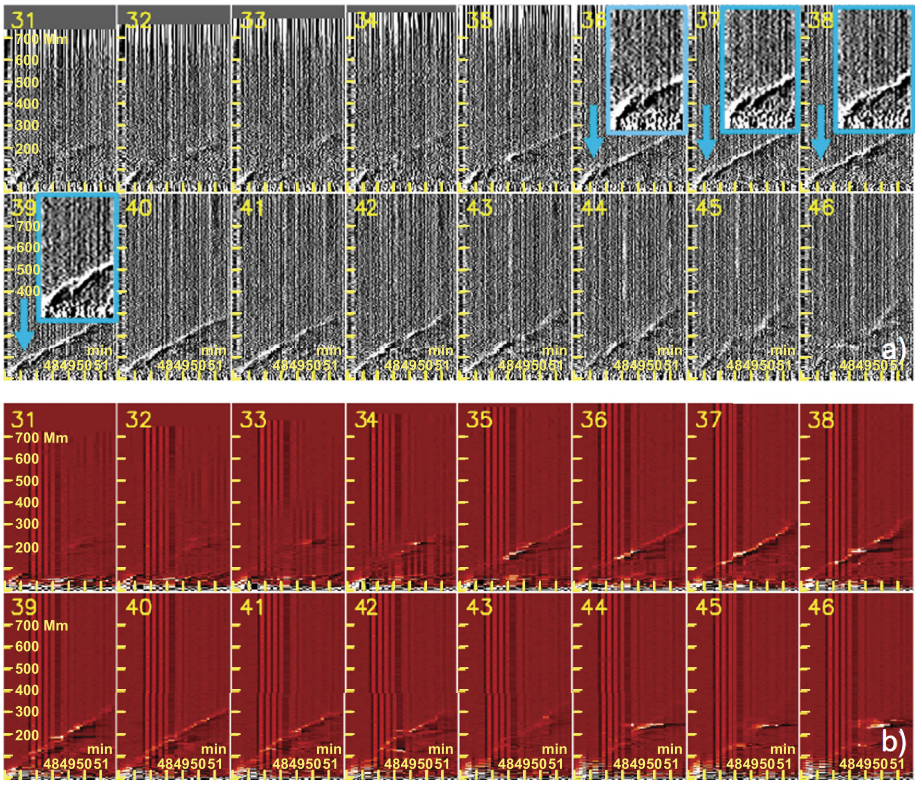

Figure 2 Stack plots of sectors 31 to 46. (a) Corresponds to Hα. The insets in the panels for sectors 36 to 39 show enlargements of the portion of the figure pointed out by a light blue arrow. (b) Corresponds to He II. The abscissae represent the time and the ordinates the distance [d_c] from the RP. The field of view is 850 Mm × 420 s. The time ranges from 17:45:00 UT to 17:52:00 UT.

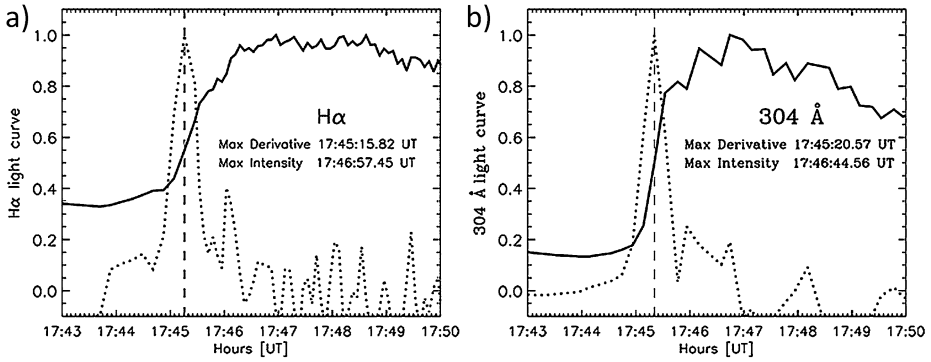

Figure 3 Flare intensity (solid line) and its derivative (dotted line) for (a) Hα and (b) He II images. The curves are normalized to their maximum intensity. The peak times of the derivative curves are indicated with a vertical dashed line. We choose the peak time of the Hα derivative curve, $t = 17{:}45{:}15.82$ UT as the reference flare onset time [$t_{on} = 17{:}45{:}16$ UT].

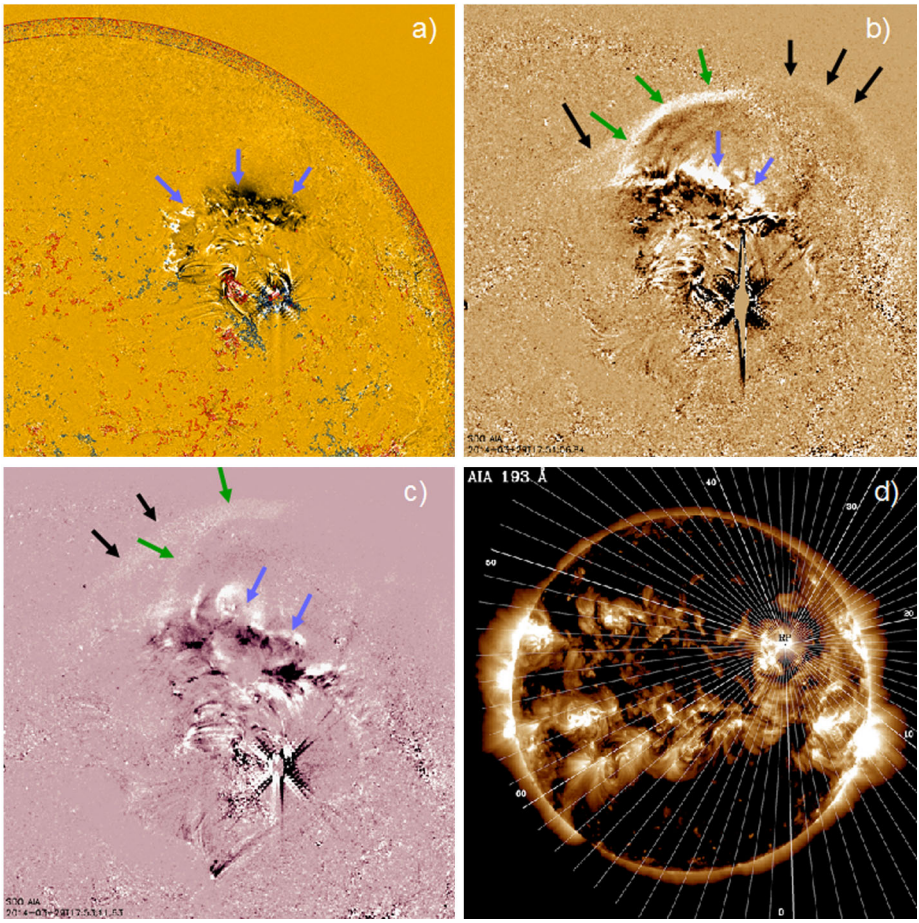

Figure 4 Snapshots of the event in the low corona. (a) Running-difference image from AIA 171 Å at 17:50:23 UT, with HMI contours ± 100 and ± 500 G superimposed (blue/red corresponds to positive/negative values) (see Movie-171). (b) Running-difference image from AIA 193 Å at 17:51:06 UT (see Movie-193). (c) Running-difference image from AIA 211 Å at 17:53:11 UT (see Movie-211). (d) Full-disk direct image from AIA 193 Å with sectors traced under a plane-of-sky assumption. We have numbered some of the 72 defined sectors. The black arrows in panels b and c indicate the faster shock, the green arrows a slower shock-like propagating feature, and the light blue arrows a propagating perturbation closer to the solar surface (see also panel a).

this panel indicate a northward-propagating arc-like disturbance that we associate with the chromospheric Moreton-wave event described in Section 3.1.

Figures 4b and 4c exhibit a tenuous circular-shaped propagating feature denoted by black arrows. The running-difference 193 Å and 211 Å images appear similar, with this feature surpassing the solar disk. This structure can be associated with an MHD coronal wave- or shock-front that likewise propagates in all directions. A second slower and circular feature indicated with green arrows in the same panels is also noticeable. This might be a secondary shock, but it could also be attributed to the leading edge of the expanding CME, as suggested by Patsourakos and Vourlidas (2012). Light blue arrows in Figures 4b and 4c indicate more irregular propagating features that show correspondence with these fronts, also pointed out

with light blue arrows in Figure 4a. They could be ascribed to an origin closer to the solar surface. They are probably caused by the interaction of the shock fronts at transition region levels or by effects of the lateral expansion of the CME bubble during its ejection. The analysis of the kinematics of the various fronts in Section 4 is helpful to validate some of these hypotheses.

To follow and characterize the visible fronts in the plane of view, we now track the evolution of the wavefronts in the plane-of-sky frame. To accomplish this, we built a new set of stack plots obtained from a plane-of-sky measurement scheme, obtaining the intensity profiles in a similar way as described in Section 3.1, *i.e.* discretizing in linear steps of ~ 1215 km along the corresponding straight path that bisects the sectors, starting from the RP. Each discrete value was computed by averaging the intensity values laterally over an angular sector of 5° centered on the RP. To ensure that the surface and plane-of-sky frames coincide, we traced the plane-of-sky bisector for each sector to match the solar-surface great circle tracing at some points P distant $\alpha = 1^\circ$ from the RP, where α is the angle subtended between the two radial vectors formed by the pairs of points (O, RP) and (O, P), as defined above. The resulting sector tracing of the plane-of-sky frame can be observed in Figure 4d.

The plane-of-sky DT-maps obtained by stacking the intensity profiles of the 193 Å band for various sectors can be observed in Figure 5. Each panel of the mosaic is the DT map of a specific sector, but in this case the DT-map ordinates exceed the solar limb, which is indicated by a horizontal white line in the different panels. Although the wave event is visible in sectors 10 to 47, we only show it from sector 16 onward in this figure. The wave feature appears brighter in sectors 35 to 44, where it has an angular span of approximately 45° toward the north. Figure 5 shows the following:

- The first visible perturbation is a well-defined bright front with an initial rising slope that is nearly constant, which tends to decelerate far from the RP. The front surpasses the limb, indicating it propagates out of the Sun. This well-defined thin front can be associated with a shock that compresses the coronal medium as it propagates, producing an EUV emission enhancement. Close to the RP it is hard to discern the front because of the flare intensity effects that disturb the observation. This shock front would correspond to the borderline of a 3D dome-shaped structure, evolving outward in the corona.
- The slopes of the first front are similar but not equal in the different panels, suggesting an angular dependence of the shock-front speed. This could be attributed to inhomogeneities of the coronal environment where the wave propagates, but a line-of-sight projection of the 3D dome-shaped structure or a particular behavior of the 3D piston that generates the shock wave are also possible.
- After the shock, some bright and complex propagating structures are visible in all of the displayed sectors. It is possible to see that these features, initially cospatial, detach from the shock front at a certain distance from the RP (see panels for sectors 35 to 45). This can be attributed to near-surface EUV waves.
- Some diffuse features, slower than the shock but faster than the bright structures, surpass the solar limb in the panels for sectors 30 to 32, which may be indicative of an outward propagation. These features probably correspond to some CME parts that are visible during its lift-off, but other true MHD waves cannot be ruled out.

3.3. White-Light Counterpart

The CME associated with the low-coronal event was first seen at 18:12 UT with the C2 coronagraph of the *Large Angle and Spectroscopic Coronagraph* (LASCO: Brueckner *et al.*, 1995) onboard SOHO. Initially, it appeared as a bright front toward the

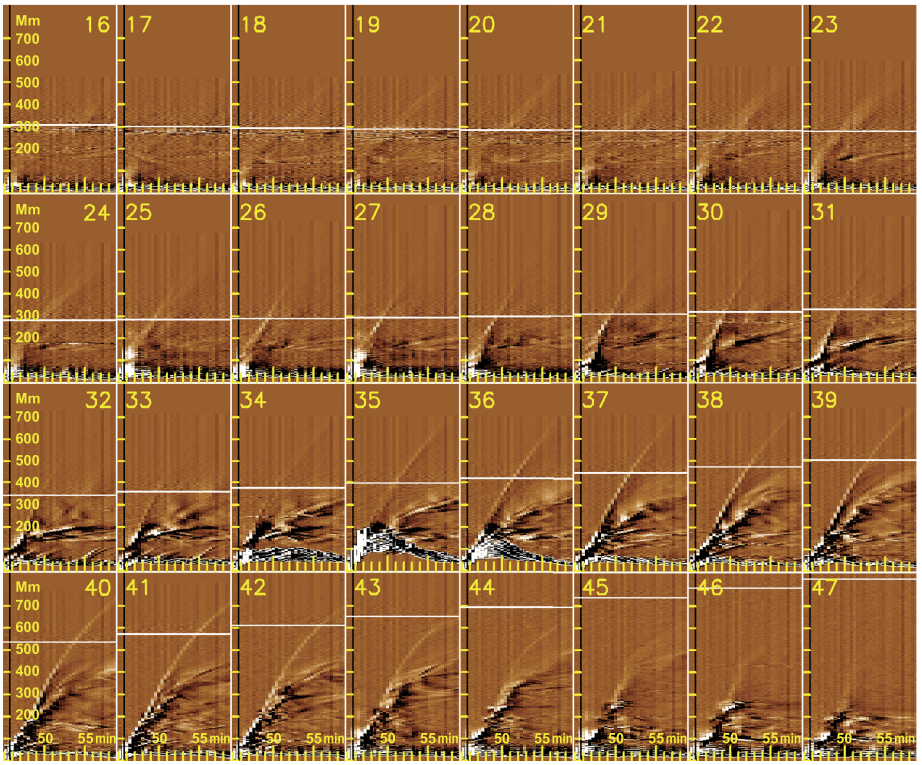

Figure 5 Stack plots for sectors 16 to 47 from AIA 193 Å in the plane-of-sky frame. The abscissae represent the time and the ordinates distance [d_s] from the RP. The time ranges from $t = 17{:}45{:}00$ UT to $t = 17{:}59{:}00$ UT. The dimensions of each panel are 850.3 Mm × 840 s. The vertical black line indicates the reference flare time. The horizontal white line in each stack plot indicates the solar-limb position.

north–west. The CME quickly evolved to become a full-halo CME with its main bulk also to the north–west (see Figure 6a). According to the SOHO LASCO CME Catalog (http://cdaw.gsfc.nasa.gov/CME_list/), the projected speed of its fastest front at a position angle of 324° after a linear fit is 528 km s^{-1}, with the most distant points showing a slightly decelerated profile. The STEREO spacecraft were located almost at the opposite side of Earth, separated by almost 42°, as shown in the cartoon in Figure 6b. From the viewpoint of the COR2 coronagraph onboard STEREO-B, the CME appears nearly symmetric (Figure 6c) but with its main bulk towards the north. From the perspective of STEREO-A, the CME appears as a partial halo traveling toward the northwest (Figure 6d). With these stereoscopic considerations, the 3D propagation direction of the CME is obtained by means of the forward model developed by Thernisien, Vourlidas, and Howard (2009). The deduced direction is N37 W34, suggesting a northward deflection of $\approx 27°$ when we consider the source region at the RP coordinates (N10.3 W32.8).

We interpret the outermost rim of the CME as indicative of a shock wave ahead of the CME bulk, as done by Ontiveros and Vourlidas (2009). To enhance the shock signatures, which are fainter than the bulk of the CME, we produced sequences of running-difference images. The CME shock can be discerned from the much brighter CME material, not only because it is fainter, but also because it appears as a distinct somewhat circular and con-

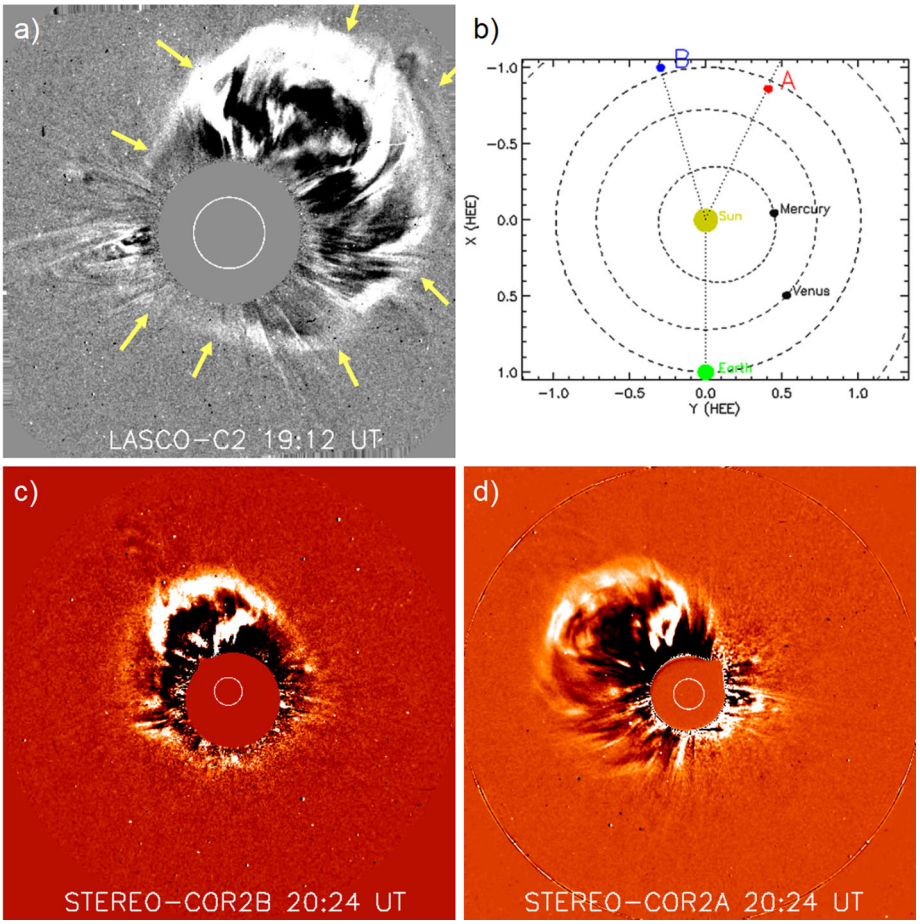

Figure 6 The associated CME as viewed by the coronagraphs LASCO from Earth's perspective and the two COR2 from the STEREO spacecraft vantage points. (a) LASCO C2 running-difference image with arrows indicating the shock driven by the CME. (b) Relative locations of the spacecraft as shown by the tool "Where is STEREO" at the STEREO Science Center (http://stereo-ssc.nasa.gov). (c) Running-difference image from COR2 on STEREO-B. (d) Running-difference image from COR2 on STEREO-A.

tinuous rim that envelops the CME bulk, which is usually off-center because of projection effects. Toward the northwest in Figure 6a, the CME leading edge meets the shock, while especially to the east and south the only observable feature is the shock, as indicated by the arrows. In a similar manner, in the STEREO-B COR2 image (Figure 6c) the bulk of the CME travels toward the north, while to the west, south, and east only the shock is evident. STEREO-A COR2 also shows the shock wave, but to the southeast, in agreement with the CME propagation direction and the spacecraft locations. An interpretation of these images to find correspondences between the CME and solar features is attempted in Section 4.4.

4. The Kinematics of the Moreton and EUV Waves

To measure the locations of the wavefronts in the DT maps obtained from the surface-frame and the plane-of-sky assumptions, we applied a visual method to identify and select the

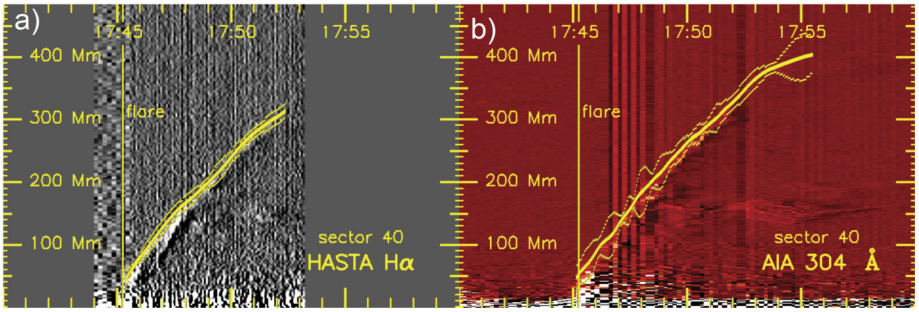

Figure 7 Sample DT map for sector 40 (d_c *vs.* time). (a) Corresponds to HASTA data. (b) Corresponds to AIA 304 Å data. The average spline is drawn with a thick yellow line and outlines the fastest front. The thin yellow lines at both sides mark an error band at 3 σs. The vertical yellow line indicates the flare onset time.

bright traces given that the fronts exhibit a non-homogeneous and diffuse pattern, especially away from the RP. This task was performed on each DT map by manually selecting several points belonging to the leftmost side of the bright trace outline, *i.e.* the features of the traveling perturbation that appear first in time. These points were then connected by means of a spline to build a profile that represents the temporal evolution of the distance [d_c]. To minimize errors, the procedure was repeated at least five times, obtaining an average spline for each of the sectors of interest. As an example, Figure 7 shows the average splines obtained under the surface-frame assumption for sector 40 for Hα (panel a) and He II (panel b) superimposed on the DT map. The thin yellow lines at both sides of the thick line mark the error band at $\pm 3\,\sigma$s.

4.1. Surface Velocity

We estimated the kinematic characteristics of the Moreton wavefronts by fitting power-law curves (Warmuth *et al.*, 2004a; Francile *et al.*, 2013) for every sector of interest to the average spline obtained, as indicated above. These curves are suitable to smoothly fit kinematic trajectories with non-constant accelerations. The power-law is given by

$$d(t) = c_1 (t - t_0)^{\delta} + c_2, \tag{1}$$

where t_0 is given the arbitrary value of 17:30:00 UT. To understand the kinematic evolution, the instantaneous values of speed and acceleration were evaluated at the flare onset time t_{on} = 17:45:16 UT and at a subsequent time t = 17:50:00 UT using the following equations:

$$v(t) = c_1 \delta (t - t_0)^{(\delta - 1)}, \tag{2}$$

$$a(t) = c_1 \delta (\delta - 1)(t - t_0)^{(\delta - 2)}. \tag{3}$$

The instantaneous values obtained from the Hα and He II data are listed in Tables 1 and 2, respectively. The mean values listed in the tables were obtained by averaging the sectors in which the wave is brighter, *i.e.* sectors 35 to 43.

In both tables the accelerations are negative with an absolute value that decreases with time, which indicates that the wave tends to slow down with a non-constant deceleration. The absolute values obtained from He II data are on average similar to those from Hα, in regard to both acceleration and speed. The initial speeds of the Moreton front derived from Hα at t_{on} (Table 1) vary in the range 570 – 925 km s^{-1}, disregarding the deviating value of sector 31. The wave speed decays to approximately 500 – 830 km s^{-1} five minutes later.

Table 1 Accelerations and speeds of the wavefront derived from Hα observations using a power-law fit. The last two rows display the acceleration and speed obtained by applying a power-law fit to the CorPITA results and our sector 36 in the same time range (17:46:52 UT to 17:52:27 UT), which we have called 36*.

Hα sector	Acceleration [km s^{-2}]		Speed [km s^{-1}]	
	t_{on} = 17:45:16 UT	t = 17:50:00 UT	t_{on} = 17:45:16 UT	t = 17:50:00 UT
31	-0.248 ± 0.008	-0.166 ± 0.005	461.2 ± 16.5	403.7 ± 14.7
32	-0.297 ± 0.006	-0.199 ± 0.004	569.6 ± 12.2	500.7 ± 10.9
33	-0.305 ± 0.011	-0.207 ± 0.008	633.2 ± 26.9	562.1 ± 24.3
34	-0.298 ± 0.009	-0.201 ± 0.006	602.9 ± 19.9	533.5 ± 17.9
35	-0.292 ± 0.004	-0.197 ± 0.003	584.1 ± 9.3	516.2 ± 8.3
36	-0.314 ± 0.004	-0.212 ± 0.002	649.7 ± 8.7	576.5 ± 7.8
37	-0.304 ± 0.006	-0.207 ± 0.004	640.1 ± 15.1	569.0 ± 13.6
38	-0.363 ± 0.006	-0.247 ± 0.004	779.0 ± 14.6	694.1 ± 13.2
39	-0.354 ± 0.005	-0.241 ± 0.003	779.2 ± 11.9	696.4 ± 10.8
40	-0.399 ± 0.005	-0.265 ± 0.003	722.1 ± 9.3	629.9 ± 8.2
41	-0.350 ± 0.005	-0.237 ± 0.004	724.0 ± 12.5	642.3 ± 11.3
42	-0.345 ± 0.005	-0.234 ± 0.003	715.1 ± 10.9	634.7 ± 9.8
43	-0.388 ± 0.005	-0.264 ± 0.004	823.5 ± 13.2	732.8 ± 11.9
44	-0.396 ± 0.006	-0.269 ± 0.004	850.2 ± 14.3	757.6 ± 13.0
45	-0.422 ± 0.007	-0.288 ± 0.005	925.6 ± 19.1	826.8 ± 17.4
46	-0.418 ± 0.003	-0.285 ± 0.002	909.8 ± 8.2	812.0 ± 7.4
Mean	-0.345 ± 0.036	-0.234 ± 0.024	713.0 ± 76.7	632.4 ± 69.6
CorPITA	-0.332 ± 0.001	-0.226 ± 0.001	718.4 ± 3.8	640.7 ± 3.4
36*	-0.306 ± 0.004	-0.208 ± 0.003	659.1 ± 9.2	587.6 ± 8.3

To validate these measurements, we applied the automated Coronal Pulse Identification and Tracking Algorithm (CorPITA: Long *et al.*, 2014) to HASTA Hα data. CorPITA identifies the wave over the highest-rated arc, *i.e.* 356° counterclockwise from solar north in the images, between 17:46:52 UT to 17:52:27 UT. To enable comparisons, we performed a power-law fit in the previously mentioned time interval to the distance–time CorPITA results and to our sector 36. This sector is coincident with CorPITA's highest-rated arc; we recall that sector 0 is centered on the great circle that crosses the solar South Pole. The obtained values are listed at the bottom of Table 1, where we indicated as sector 36* the results of the power-law fit to our data in the same time interval when CorPITA detects the wave. The acceleration and speed values obtained from CorPITA and our measurements differ by ≈ 9 %.

The different measurement methods, curve fitting, and error treatments will eventually translate into differing results. We applied a visual method to track the leading edge of the perturbations on running-difference images. Instead, the CorPITA code uses a Gaussian fit for the perturbation profiles, which is applied to percentage base-difference images to track the center of the Gaussian curves. Thus, the position of the wavefront measured by CorPITA is always delayed with respect to the leading edge of our measurements. The mean distance between the two fitted curves in the time range 17:46:52 UT to 17:52:27 UT is 18.5 Mm, which is consistent with half of the thickness of the Hα pulses reported by Warmuth *et al.* (2004b) after analyzing several Moreton wave events; this thickness is in the range $\approx 40-70$ Mm.

Table 2 Accelerations and speeds derived from 304 Å observations using a power-law fit.

Sector 304 Å	Acceleration [km s^{-2}]		Speed [km s^{-1}]	
	t_{on} = 17:45:16 UT	t = 17:50:00 UT	t_{on} = 17:45:16 UT	t = 17:50:00 UT
31	-0.343 ± 0.008	-0.233 ± 0.006	714.6 ± 19.5	634.6 ± 17.6
32	-0.341 ± 0.004	-0.229 ± 0.003	653.7 ± 9.5	574.5 ± 8.5
33	-0.284 ± 0.003	-0.187 ± 0.002	488.5 ± 6.0	423.1 ± 5.3
34	-0.363 ± 0.005	-0.236 ± 0.004	571.1 ± 9.5	488.1 ± 8.2
35	-0.321 ± 0.006	-0.217 ± 0.004	655.0 ± 14.8	580.2 ± 13.3
36	-0.336 ± 0.006	-0.228 ± 0.004	701.1 ± 15.2	622.6 ± 13.8
37	-0.354 ± 0.006	-0.241 ± 0.004	753.5 ± 14.8	670.7 ± 13.4
38	-0.352 ± 0.007	-0.238 ± 0.005	726.4 ± 16.2	644.2 ± 14.6
39	-0.405 ± 0.007	-0.272 ± 0.005	785.6 ± 15.7	691.5 ± 14.0
40	-0.356 ± 0.006	-0.239 ± 0.004	694.5 ± 13.2	611.7 ± 11.9
41	-0.371 ± 0.007	-0.249 ± 0.005	705.5 ± 15.6	619.4 ± 13.9
42	-0.405 ± 0.006	-0.268 ± 0.004	708.9 ± 12.2	615.3 ± 10.7
43	-0.387 ± 0.004	-0.260 ± 0.003	742.3 ± 8.7	652.5 ± 7.8
44	-0.413 ± 0.012	-0.281 ± 0.008	896.1 ± 29.8	799.6 ± 27.0
45	-0.337 ± 0.010	-0.234 ± 0.007	860.8 ± 30.2	781.2 ± 27.9
46	-0.409 ± 0.017	-0.279 ± 0.012	894.2 ± 44.4	798.5 ± 40.3
Mean	-0.365 ± 0.029	-0.246 ± 0.018	719.2 ± 37.9	634.2 ± 33.9

On the other hand, although more appropriate for tracking the leading edge of the wavefront, the visual method combined with a spline interpolation over few points is an inherently high-error procedure. While the CorPITA code tracks the wavefront center, it uses a more reliable procedure that allows for a better error treatment. Moreover, we used angular sectors to average the intensities along paths that emanate from the RP, while CorPITA obtains the profiles from constant width paths, which would lead to disagreements far from the RP because of probable inhomogeneities of the wavefront. Furthermore, the intensity profile of a shock wave decays and broadens with time (Warmuth *et al.*, 2004b). In consequence, the kinematics determined from measuring the leading edge differ from those deduced from the center of the intensity profile. This could explain the higher deceleration value obtained from the CorPITA results listed in Table 1.

4.2. Plane-of-Sky Velocity

We applied the same procedure as in Section 4.1 to obtain curves representative of the evolution of the shock fronts in the low corona, *i.e.* in the plane-of-sky frame. The DT maps from AIA 193 Å sectors 35, 37, 39, 41, 43, and 45 are displayed in Figure 8 with the average splines obtained with the visual method superimposed in white. For comparison, we also determined the splines from Hα and AIA 304 Å in the plane-of-sky frame. These are represented by the yellow and red lines in the same figure, respectively.

We obtained the kinematic characteristics of the shock wavefront in each sector for AIA 193 Å in the same way as in Section 4.1, *i.e.* by fitting power-law curves to the average splines in the full temporal range. The results are presented in Table 3; we calculated the instantaneous acceleration and speed values for the times t_{on} = 17:45:16 UT and t = 17:50:00 UT.

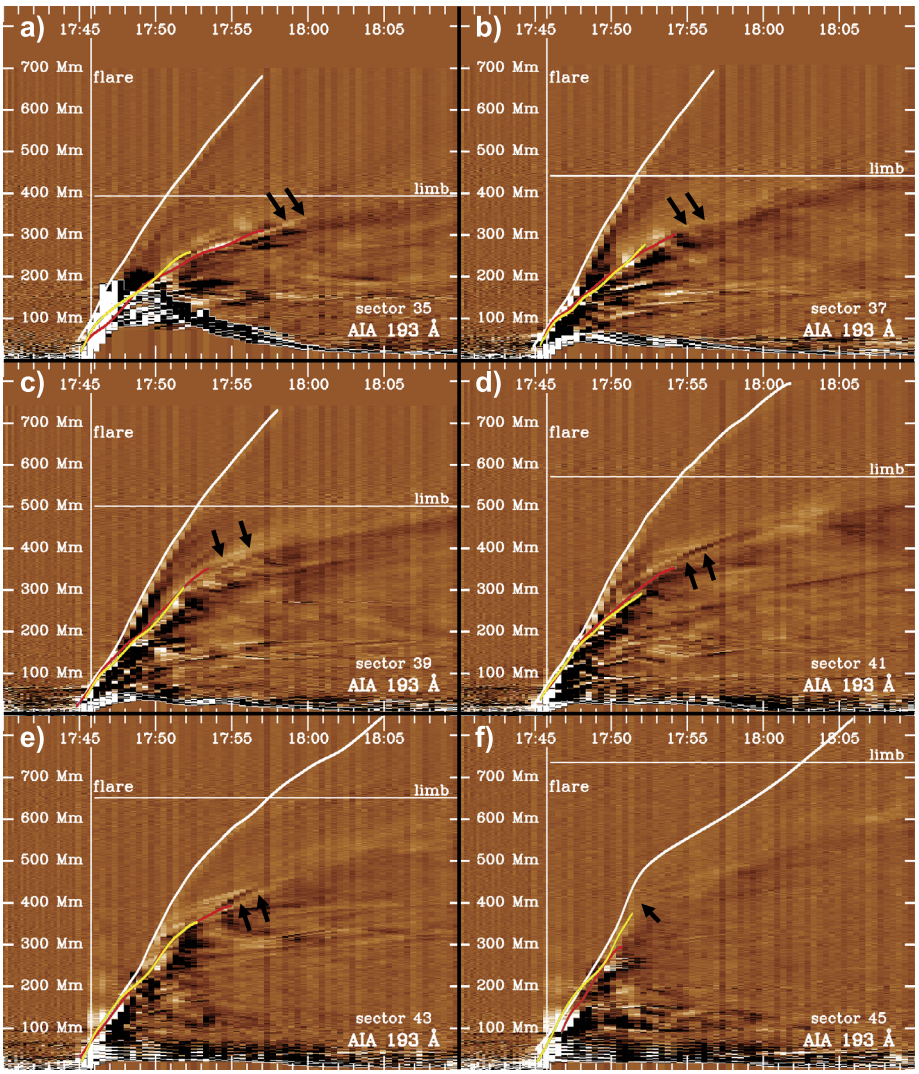

Figure 8 DT maps determined from AIA 193 Å data with superimposed splines in the plane-of-sky frame outlining the temporal evolution (d_s *vs.* time) of various features: the fastest front detected with AIA 193 Å (white line), the Moreton wavefront recorded by HASTA (yellow line), and the wavefront detected by AIA 304 Å (red line). The black arrows denote bright coronal features that appear to persist after the traces derived from chromospheric data end. From left to right and top to bottom, the panels correspond to sectors 35, 37, 39, 41, 43, and 45.

4.3. Coronal Wave Model

To investigate the angular dependence of the wave evolution in the plane-of-sky view, we built an (x, y) plot based on the shock-front curves obtained from AIA 193 Å data. In this plot, increasing x corresponds to the east–west direction and increasing y to the south–north direction. This graph was obtained by plotting the d_s distances every 15 s from the RP, derived from the average splines along the corresponding trajectories previously used to

Table 3 Accelerations and speeds derived from 193 Å observations using a power-law fit.

Sector 193 Å	Acceleration [km s^{-2}]		Speed [km s^{-1}]	
	t_{on} = 17:45:16 UT	t = 17:50:00 UT	t_{on} = 17:45:16 UT	t = 17:50:00 UT
16	-0.235 ± 0.012	-0.162 ± 0.008	589.5 ± 35.1	534.2 ± 32.4
17	-0.389 ± 0.010	-0.258 ± 0.007	687.5 ± 20.3	597.6 ± 17.9
18	-0.335 ± 0.007	-0.225 ± 0.005	651.2 ± 16.5	573.5 ± 14.7
19	-0.349 ± 0.008	-0.235 ± 0.005	682.2 ± 17.6	601.1 ± 15.8
20	-0.455 ± 0.008	-0.302 ± 0.005	812.1 ± 16.0	707.1 ± 14.1
21	-0.573 ± 0.008	-0.370 ± 0.005	844.5 ± 13.3	713.9 ± 11.4
22	-0.558 ± 0.011	-0.363 ± 0.007	856.5 ± 18.2	728.8 ± 15.7
23	-0.422 ± 0.007	-0.286 ± 0.005	888.2 ± 17.3	789.6 ± 15.6
24	-0.419 ± 0.010	-0.285 ± 0.007	912.9 ± 25.9	814.9 ± 23.5
25	-0.416 ± 0.008	-0.285 ± 0.005	956.2 ± 20.5	858.7 ± 18.7
26	-0.432 ± 0.008	-0.296 ± 0.006	999.1 ± 21.7	897.7 ± 19.8
27	-0.412 ± 0.009	-0.283 ± 0.006	976.5 ± 25.1	879.7 ± 22.9
28	-0.465 ± 0.008	-0.318 ± 0.006	1045.0 ± 21.3	936.0 ± 19.4
29	-0.500 ± 0.010	-0.342 ± 0.007	1144.9 ± 26.2	1027.6 ± 23.9
30	-0.524 ± 0.008	-0.360 ± 0.005	1217.6 ± 20.6	1094.5 ± 18.8
31	-0.534 ± 0.001	-0.366 ± 0.001	1241.4 ± 3.9	1116.0 ± 3.6
32	-0.527 ± 0.008	-0.361 ± 0.006	1214.6 ± 22.8	1090.9 ± 20.8
33	-0.550 ± 0.007	-0.375 ± 0.005	1205.2 ± 17.5	1076.4 ± 15.9
34	-0.683 ± 0.008	-0.445 ± 0.005	1070.7 ± 13.2	914.3 ± 11.4
35	-0.566 ± 0.007	-0.376 ± 0.005	1001.2 ± 14.3	870.5 ± 12.6
36	-0.571 ± 0.005	-0.382 ± 0.004	1071.1 ± 11.6	938.7 ± 10.3
37	-0.494 ± 0.006	-0.336 ± 0.004	1077.6 ± 14.0	962.1 ± 12.7
38	-0.494 ± 0.005	-0.336 ± 0.004	1067.4 ± 13.2	951.8 ± 11.9
39	-0.577 ± 0.007	-0.387 ± 0.005	1102.1 ± 14.6	968.3 ± 13.0
40	-0.679 ± 0.005	-0.444 ± 0.003	1083.4 ± 8.8	927.8 ± 7.6
41	-0.512 ± 0.004	-0.343 ± 0.002	963.6 ± 7.7	844.8 ± 6.9
42	-0.533 ± 0.004	-0.351 ± 0.003	883.8 ± 7.2	761.1 ± 6.3
43	-0.518 ± 0.006	-0.339 ± 0.004	830.8 ± 10.2	712.0 ± 8.9
44	-0.546 ± 0.003	-0.353 ± 0.002	808.6 ± 5.6	684.1 ± 4.8
45	-0.370 ± 0.005	-0.246 ± 0.003	675.1 ± 10.0	589.6 ± 8.9
46	-0.446 ± 0.007	-0.295 ± 0.005	770.9 ± 14.0	668.1 ± 12.3
47	-0.381 ± 0.031	-0.267 ± 0.022	1109.0 ± 110.6	1018.5 ± 103.2
Mean	-0.483 ± 0.097	-0.324 ± 0.062	951.3 ± 181.4	839.1 ± 168.3

define the sectors, from t_{on} = 17:45:16 UT to t = 17:55:46 UT. The resulting wavefronts are shown in Figure 9. Several characteristics of the shock evolution are evident:

- A fairly homogeneous circular pattern is observed between sectors 16 and 45, which would indicate the evolution of a quasi-circular coronal front in the plane-of-sky view. This front might be interpreted as the borderline of a quasi-spherical 3D-dome EUV wave evolving toward the observer.

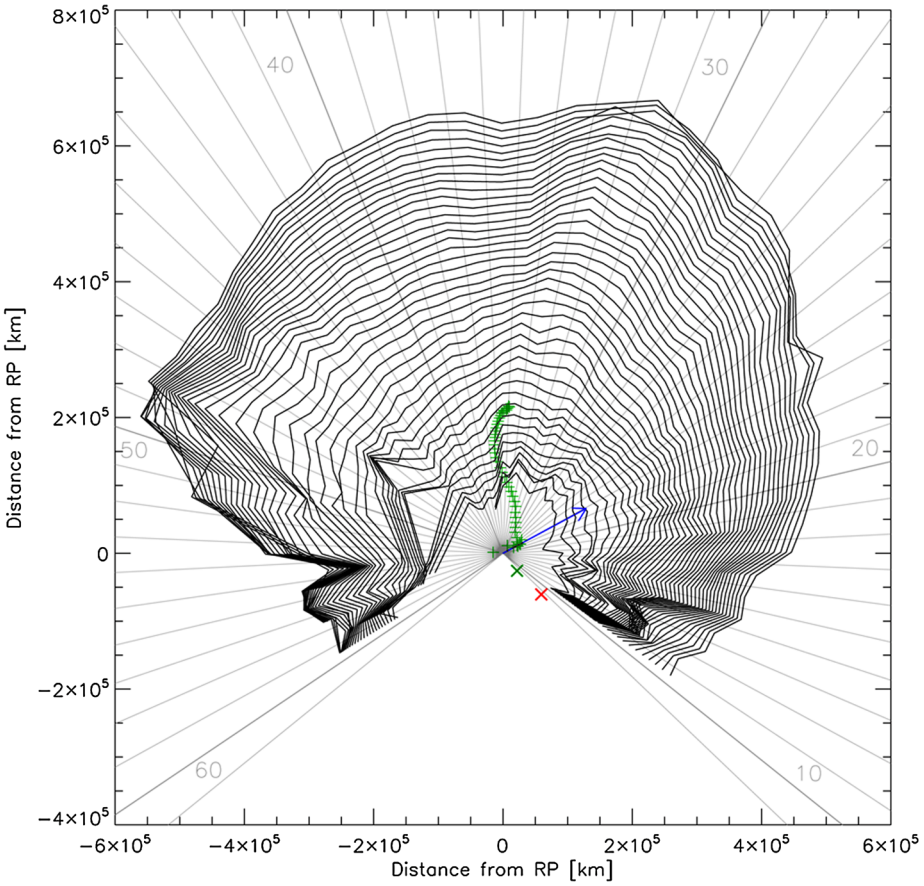

Figure 9 An (x, y) plot showing the angular dependence of the AIA 193 Å wave evolution in the plane-of-sky view. The wavefronts are obtained from the set of points determined from the average splines for each sector. Some sectors are labeled. Sectors depart from the location originally defined as the RP. The curves are traced every 15 s, from $t_{on} = 17{:}45{:}16$ UT to $t = 17{:}55{:}46$ UT. The green + signs indicate the wavefront centers. The blue arrow is the projection on the plane of view of a vector normal to the surface at the RP coordinates. The x signs indicate the extrapolated centers of the circumferences to the reference flare time, with green corresponding to a linear fit and red to a quadratic fit.

- Between sectors 29 and 34, however, the wavefront exhibits a lobe, suggesting that it moves faster in this region than in the remaining sectors. This is in agreement with the initial speed values listed in Table 3.
- Southward of AR 12017, no shock wave is detected, probably because the high Alfvén speed in the AR inhibits the shock formation and propagation (Vršnak and Cliver, 2008). To either side of the AR (sectors 10 – 15 and 49 – 59) the shock exhibits an irregular pattern. This is probably the result of a more diffuse and less intense shock front in these sectors, thus implying higher measurement errors.
- The entire circular pattern appears to move northward, as indicated by the green plus signs that denote the locations of the centers of every wavefront. These were determined by interpolating circumferences to the wavefronts (see the following paragraphs), taking into account all sectors between 16 and 45.

Table 4 Coefficients for the linear (b and c) and quadratic (a, b, and c) fittings of the circumference centers and radii with time. Time zero was set to the flare onset time, $t_{on} = 17{:}45{:}16$ UT.

Fit	a [km s^{-2}]	b [km s^{-1}]	c [km]
x linear	–	-4.923×10^{1}	2.172×10^{4}
x quadratic	0.327	-2.947×10^{2}	5.935×10^{4}
y linear	–	4.211×10^{2}	-2.574×10^{4}
y quadratic	−0.328	6.573×10^{2}	-6.073×10^{4}
Radius linear	–	6.001×10^{2}	1.040×10^{5}
Radius quadratic	−0.279	8.050×10^{2}	7.643×10^{4}

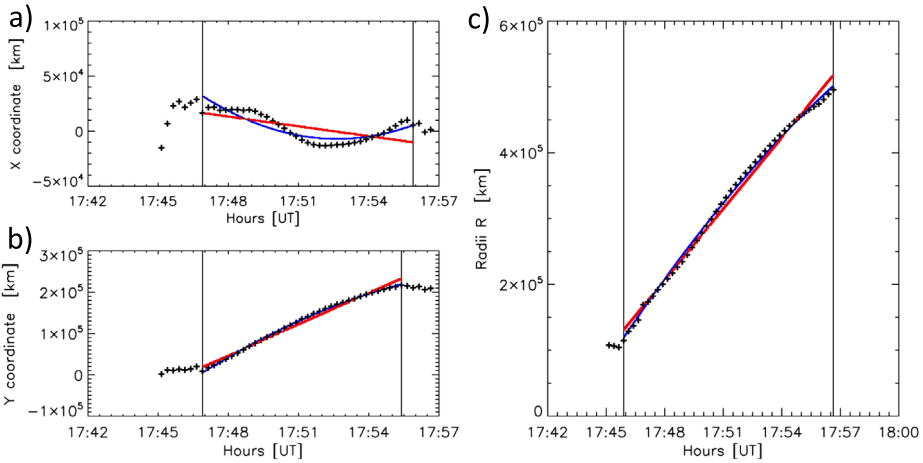

Figure 10 Temporal evolution of the parameters deduced from interpolating circumferences to the wavefronts including sectors between 16 and 45. (a) Corresponds to the x-coordinate of the centers of the circumferences. (b) Shows the y-coordinate of the centers. (c) Corresponds to the radii of the circumferences. In all panels the vertical black lines delimit the region where the points are fitted by curves. The red and blue lines represent the linear and quadratic fits, respectively.

- The bulk of the 3D-dome EUV wave does not follow the radial direction, as shown by the blue arrow, which indicates the plane-of-view projection of a radial vector located at the RP.

To obtain the general characteristics of the shock evolution, we interpolated circumferences to the shock fronts that evolve in time, as displayed in Figure 9. For the fitting we used a Levenberg-Marquardt reliable algorithm from the MPFIT libraries (Markwardt, 2009). The centers of the interpolated circumferences are superimposed in Figure 9 as green plus signs. They show a pronounced northward drift with time, which slightly oscillates in the east–west direction.

The results of the interpolation can be observed in Figure 10. Panel a shows the evolution in time of the x coordinate of the inferred circumference centers. The red and blue lines in this panel are the linear and quadratic fits to the points within the range indicated by the vertical lines, neglecting the deviating data points at the beginning and end times. The evolution of the y coordinate of the circumference centers is similarly shown in panel b, where a fast displacement in this direction is evident. Panel c shows the evolution of the circumference radii, which increase with a speed of $v_r \approx 600$ km s^{-1}. The results of the fitting are listed in Table 4.

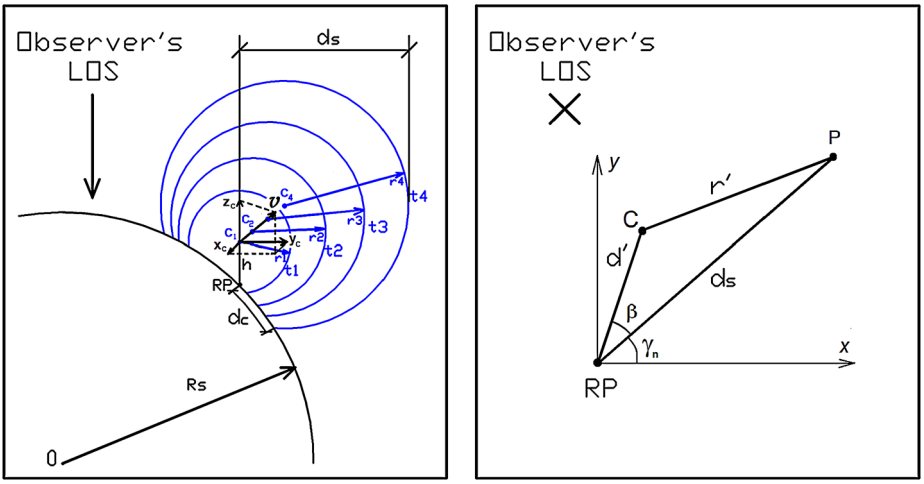

Figure 11 (a) Sketch of the coronal wave model showing the relationship between an expanding and outward-moving sphere and its chromospheric trace as it evolves in time. R_S stands for the solar radius and RP for the radiant point, d_c is the distance from the RP to the chromospheric trace, d_s is the distance from the RP to the projection of the sphere on the plane-of-view in the direction of a particular sector, and h is the height of the sphere center. (b) Scheme of the plane-of-view used to calculate the measured radius of the expanding sphere $[r']$ (see Equation (4)).

To determine the site where the wave event originates, we performed a backward extrapolation to the flare reference time $[t_{on}]$ of the x and y values, using the linear and quadratic fits of Figure 10a and 10b. The results are shown in Figure 9, where the green and red x signs indicate the (x, y) position obtained from the linear and quadratic fits, respectively. These two points do not coincide with the RP, but lie in the close vicinity of the AR.

Next, we correlated the measured coronal shock with the chromospheric Moreton traces. Several authors have suggested that Moreton waves can be explained by a 3D dome-shaped coronal shock front pushing down and sweeping the chromosphere (see references in Section 1). If this is the case, we should expect that both measurements, chromospheric and coronal, coincide when the coronal shock-front intersects the Sun's surface.

Following this hypothesis, the results obtained above by measuring the shock fronts (see Figures 9 and 10) could be assumed as the borderline in the plane-of-sky of a 3D structure, more or less regular, that propagates outward in the corona. Furthermore, this structure probably drifts northward, according to the temporal evolution of the (x, y) coordinates of the interpolated circumference centers.

We assumed a simple model for this 3D structure, namely an expanding sphere whose center drifts with constant velocity $[\boldsymbol{v} = (v_x, v_y, v_z)]$ and starts moving from a point located at a certain height $[h]$ above the RP. This model implicitly assumes a piston driver for the wave event. This piston driver is initially located in the vicinity of the AR and starts moving along a specific 3D path at a particular time $[t_0]$, close to the flare onset time $[t_{on}]$, compatible with the filament ejection and CME lift off (see *e.g.* Liu *et al.*, 2015, for a detailed analysis of the first stages of the event and Section 1 for a summary).

A sketch of this model is shown in Figure 11a. This panel shows a planar cut of the solar sphere along a great circle that includes the RP. The observer LOS is indicated in the figure. The observer is able to measure both the plane-of-sky coronal distances between the shock

and the RP $[d_s]$ and the chromospheric distances traveled by the Moreton traces over the solar surface $[d_c]$.

If the Moreton trace is generated by the shock wave sweeping the chromosphere, then the distance $d_c(t_i)$ must match the intersection of a sphere centered on the point $C(t_i) = (x_c(t_i), y_c(t_i), z_c(t_i))$ and with radius $r(t_i)$. We used t_i instead of t to reference the specific instants of time we used to define the average splines in the plane-of-sky and surface frame.

Owing to inhomogeneities in the shock front in the plane-of-sky frame shown in Figure 9, we used a measured sphere radius $[r'(t_i)]$ obtained from the distances $[d_s(t_i)]$ instead of the mean radius $[r(t_i)]$ obtained from the geometrical interpolation of Figure 10c. Furthermore, $d_s(t_i)$, corresponding to sector n in the plane-of-sky frame, must agree with $d_c(t_i)$ of sector n in the surface frame at the same time $[t_i]$. Each radius $[r']$ can be obtained from the corresponding distance $[d_s]$ as can be deduced from the schema in Figure 11b, which exhibits an (x, y) plane-of-sky view of the measured distance $[d_s]$ of a point P, the RP, and the center of the expanding spheres, all considered at the same time t_i. This view would correspond to one of the images captured during the event with the observer located in front of the figure. According to Figure 11b, when the origin is set in coincidence with the RP coordinates, from the law of cosines we obtain

$$r' = \sqrt{d'^2 + d_s^2 - 2d' d_s \cos\beta}, \tag{4}$$

where

$$d' = \sqrt{x_c^2 + y_c^2}, \tag{5}$$

and the angle β can be obtained as

$$\beta = \arctan\frac{y_c}{x_c} - \gamma_n, \tag{6}$$

where γ_n is the angle with respect to the x axis of the analyzed sector n and (x_c, y_c) are the coordinates of the center C in the plane of view. To compute the intersection of the measured shock sphere with the solar surface, we designed an algorithm that determines which of the points $P_j(t_i) = (x_j(t_i), y_j(t_i), z_j(t_i))$ of the set of distances $[d_c(t_i)]$ and sector n traced over the solar sphere, *i.e.* in the surface frame, fits the expanding sphere of radius $[r'(t_i)]$, obtained as explained above and centered on point $C(t_i) = (x_c(t_i), y_c(t_i), z_c(t_i))$. The coordinates $x_c(t_i)$, $y_c(t_i)$, $z_c(t_i)$ of the center point $C(t_i)$ are obtained as

$$x_c(t_i) = v_x \Delta_t + RP_x, \tag{7}$$

$$y_c(t_i) = v_y \Delta_t + RP_y, \tag{8}$$

$$z_c(t_i) = v_z \Delta_t + RP_z + h, \tag{9}$$

where $\Delta_t = (t_i - t_0)$.

The algorithm determines the points $P_j(t_i)$ in sector n from the following inequation

$$\left[x_j(t_i) - x_c(t_i)\right]^2 + \left[y_j(t_i) - y_c(t_i)\right]^2 + \left[z_j(t_i) - z_c(t_i)\right]^2 - r(t_i)^2 < \epsilon \tag{10}$$

for $i = 1, \ldots, l$ and $j = 1, \ldots, m$, where ϵ is the second power of an infinitesimal distance, l is the time of the measurement in seconds, and m the number of points for path n, in this case 1000.

The free parameters of the model are the values h, v_x, v_y, v_z, and the time t_0. We estimated the speeds v_x and v_y from the linear fit parameters listed in Table 4. We obtained t_0 as the average value of the roots of the interpolated quadratic curves of the average splines of sectors 16 to 47 and found that $t_0 = 17{:}44{:}06.75$ UT.

Kleint *et al.* (2015) measured the velocity of the ejected filament associated with the 29 March flare. They estimated a range of projected velocities of 130 to 230 km s^{-1} at 17:44:37 UT and 340 to 700 km s^{-1} at 17:45:13 UT. The initial filament height could not be measured by these authors because of the low Doppler signal, implying that such a low speed is characteristic of chromosphere and transition region heights. In consequence, we assumed $h = 1000$ km. As mentioned in Section 1, Liu *et al.* (2015) found an asymmetric filament eruption and determined a speed of 620 km s^{-1} at around 17:43 UT.

For the remaining free parameter $[v_z]$ we found an acceptable fit by choosing 310 km s^{-1} when varying v_z in steps of 10 km s^{-1}.

Finally, we found a reasonable fit of our model in case the sphere center is moving at a constant speed with components $v_x = -49.23$ km s^{-1}, $v_y = 421.05$ km s^{-1}, and $v_z = 310.0$ km s^{-1}.

In Figure 12, we took the DT maps built from AIA 193 Å for several sectors in the surface frame as a basis to draw various profiles. We superimposed on these DT maps the Hα and AIA 304 Å measured splines in yellow and red, respectively. They roughly delineate the behavior of the brighter front that travels behind the faint and faster shock-wave seen in the coronal lines. The results of the model, *i.e.* the deduced shock-wave intersection at the solar surface, is drawn in green. The figure shows a general good fit between our model and the Hα and He II traces, which suggests that the intersection of these spheres with the chromosphere corresponds to the Moreton and He II waves. In the western sectors 35 and 37 and beyond ≈200 Mm of the RP, the model results appear below the chromospheric traces, *i.e.* with slower surface speed (see Figure 12a – 12b), while the opposite applies for sector 43. This discrepancy is addressed in Section 5.2.

4.4. Correspondence Between EUV and White-Light Features

To understand the origin of the 3D-dome EUV wave observed in the low corona in connection with the white-light counterpart detected in coronagraphic images, we built DT plots along three different directions. The pathway of the shock wave in the low corona and that of the CME shock are shown together in Figure 13 along the central direction of sectors 29 (panel a), 40 (panel b), and 43 (panel c). In the low corona, the shock front is tracked using the DT maps constructed from AIA 193 Å and under the plane-of-sky assumption, as explained in Section 4.2 (see also Figures 5 and 8) and considering the RP as the origin of the wavefront. The central directions of sectors 29, 40, and 43 are shown as solid lines in Figure 13d. In this panel the symbols on the lines mark the positions of the shock fronts measured at different times for the three sectors. The measurements were performed under the plane-of-sky assumption as well.

The DT points derived from the low and white-light coronal data were fit using $d(t) = \sqrt{(at + b)} + c$, where the fit to the data was performed by applying the same Levenberg-Marquardt least-squares approximation as in Section 4.3. This equation was also applied by Cremades *et al.* (2015) to fit points of a distance–time plot of a CME/shock that resulted from the combination of white-light corona, interplanetary type II radio, and *in situ* data. The fit is very good both in correspondence with the fast growth of the height in the low corona and with the gradual increase registered later in the white-light corona. A quadratic equation was also applied to fit the data, but the fit was poor.

5. Discussion and Conclusions

We analyzed the Moreton-wave event on 29 March 2014 observed in Hα by HASTA using a five-second temporal cadence, together with high-resolution transition region and coronal

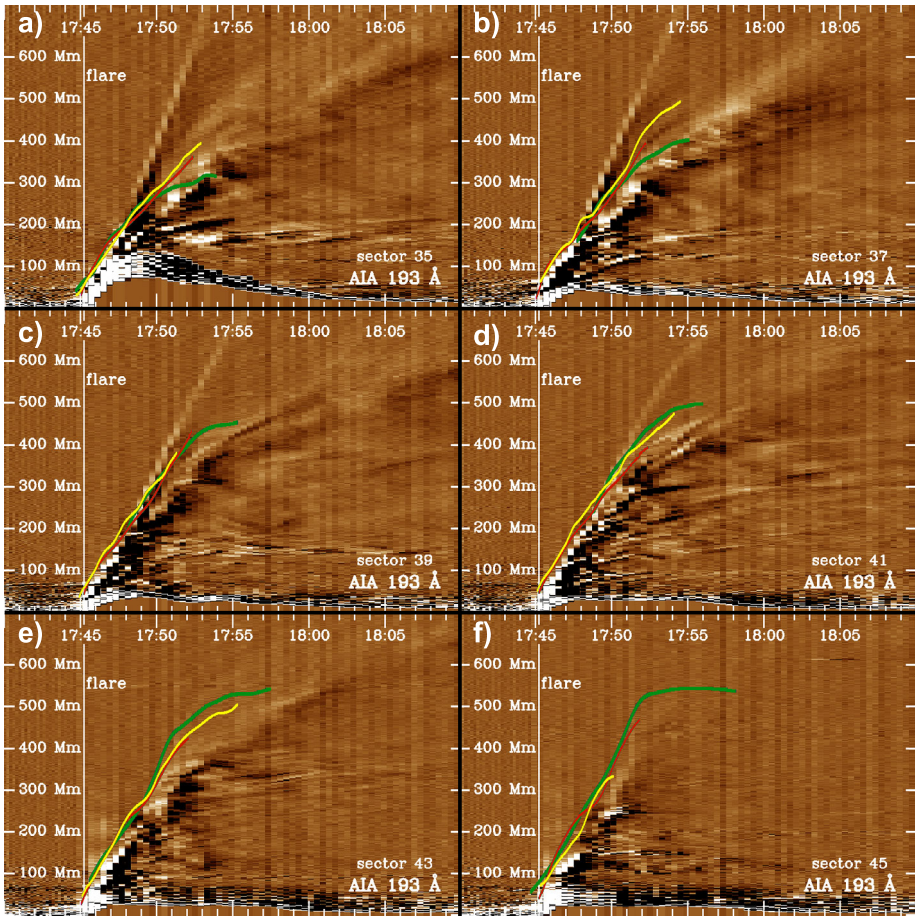

Figure 12 DT maps determined from AIA 193 Å data in the surface frame with the results from applying the coronal-wave model to a set of sectors superimposed. The green line is the modeled chromospheric trace of the fastest shock-wavefront seen in the AIA 193 Å line, while the yellow and red lines are the profiles of the wavefront in the Hα and He II lines, respectively. Panels a to f correspond to sectors 35, 37, 39, 41, 43, and 45 (from left to right and top to bottom).

EUV observations from AIA. We focused our study on the spatial behavior of the waves through a detailed analysis of the angular evolution of the wavefronts to find correspondences between the features observed in different bands and atmospheric layers. In this section we address the kinematics of the event, the correspondence found between the features detected in the various regimes, and the origin of the shocks within the blast-wave and piston-driven scenarios.

5.1. The Kinematics of the Wave Event

We first obtained the kinematic parameters of Hα and He II band wavefronts, measured on the surface frame (Section 4.1). The parameters were calculated considering an RP located at the brightest flare kernel, *i.e.* not using an RP derived from tracing arcs of circumferences

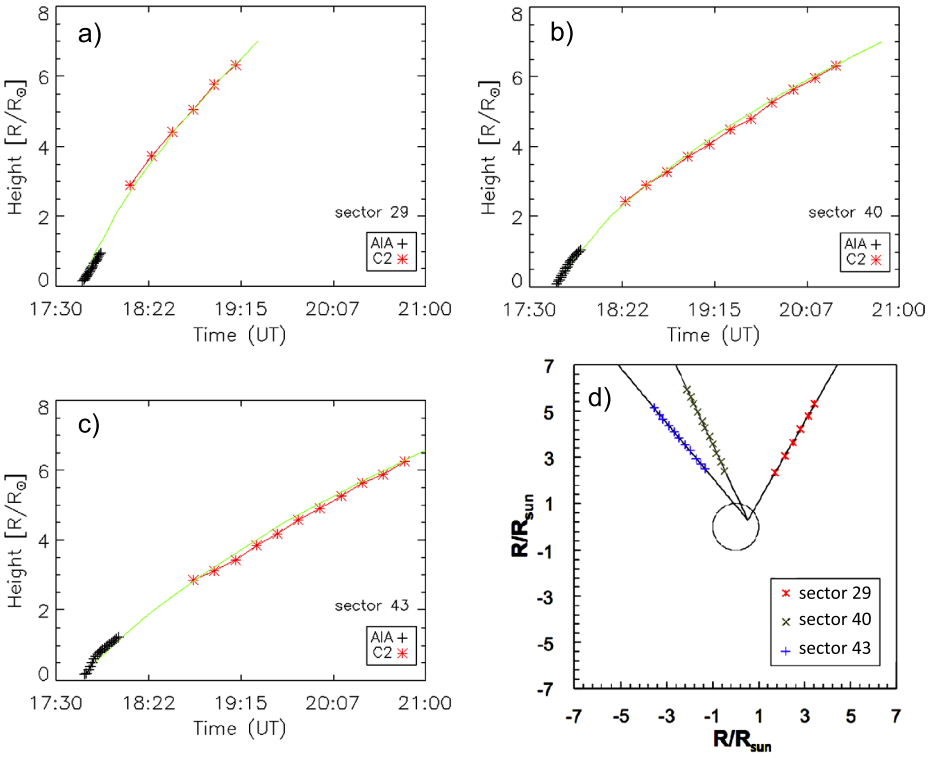

Figure 13 (a) Distance-time plot corresponding to sector 29 with black plus signs representing plane-of-sky points derived from AIA 193 Å and red asterisks plane-of-sky measurements of the CME shock. (b) Same as panel a, but for sector 40. (c) Same as panel a, but for sector 43. The green solid lines in panels a, b, and c show a fit to measurements of AIA 193 Å and LASCO C2 together (see text). (d) A plane-of-view plot indicating the three directions along which the distance–time measurements of the CME shock have been performed in LASCO C2 images, as well as the measured points. The circle represents the solar disk.

over the chromospheric Hα fronts, as done by other authors (Warmuth *et al.*, 2004a,b; Francile *et al.*, 2013). Despite the differences between the methods of measurement, we consider that the values of the kinematic parameters (distances, speeds, and accelerations) should be similar far from the AR.

The first Hα traces are detected ≈ 50 Mm away from the brightest flare-kernel site. This distance to the flare is shorter than the mean distance determined by Warmuth *et al.* (2004b) for several Moreton events. The angular extent of the chromospheric disturbance is $\approx 80°$. The Hα kinematic parameters show the typical characteristics of Moreton chromospheric waves, with initial speeds between $570-925$ km s^{-1} decaying to $500-830$ km s^{-1} five minutes later. The instantaneous accelerations determined at the flare onset time and five minutes later listed in Table 1 yield a mean initial deceleration of ≈ 0.345 km s^{-2} that decreases in absolute value with time. The analysis by sectors reveals dispersions in the speed and acceleration values, suggesting a non-homogeneous angular behavior of the Moreton wavefronts. A similar kinematic analysis performed on the He II distance–time maps shows similar values of acceleration and speed with respect to Hα. This suggests that the upper chromosphere and the transition region respond similarly to the increase in pressure or density produced by

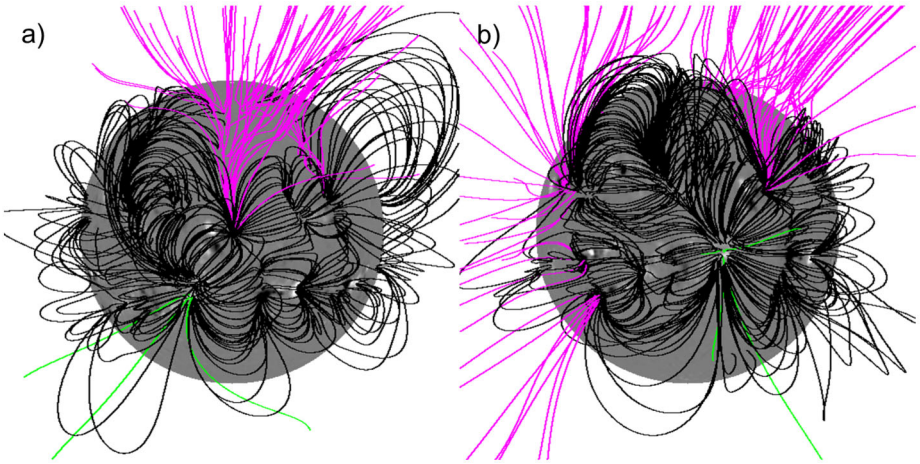

Figure 14 PFSS model for Carrington rotation 2148. (a) Shows the AR at central meridian passage. (b) Corresponds to the AR as viewed from the Earth on 29 March 2014 at 12:04:00 UT. The field-line color convention is such that black indicates closed lines and magenta (green) corresponds to open lines anchored in the negative-polarity (positive-polarity) field.

the arrival of the coronal shock, which leads to emission enhancements (Vršnak and Cliver, 2008; Leenaarts, Carlsson, and Rouppe van der Voort, 2012; Krause *et al.*, 2015).

The kinematic parameters of the shock front in the AIA 193 Å band were subsequently determined for all sectors. A directional dependence of the acceleration and speed is evident, with the highest deceleration corresponding to the zone covering sectors 28 – 44, *i.e.* the northward direction along which the Moreton fronts are observed. The visibility range could contribute to this effect given that the wave can be tracked to much larger distances for these sectors, thus allowing for the deceleration to become significant in the power-law fit. The speeds calculated ≈ 5 min after the wave ignition are in general greater than 900 km s^{-1} in sectors 28 – 40. Typical coronal values in quiet regions are $c_s = 185$ km s^{-1} for the sound speed, $v_A = 273$ km s^{-1} for the Alfvén speed, and $v_{ms} = 330$ km s^{-1} for the fast magneto-acoustic speed (Warmuth, 2015), implying for our wave a magneto-acoustic Mach number of ≈ 3, considering the shock evolving close to the solar surface, toward the north, and far from the AR. High mean deceleration rates correspond to high Mach-number values of a shock wave, whereby the wave rapidly looses energy and decelerates faster. Regardless of this fact, the speed of the wave northwards and far from the AR is still significant enough to ensure a high compression ratio at chromospheric levels to generate the Moreton wave. On the other hand, a lower Mach number is expected in the vicinity and above the AR.

The wave brightness is noticeably higher between sectors 35 – 43 in Hα and He II (see Figure 2). The fastest wavefront detected in the AIA 193 Å band comprises sectors 28 – 40. This partial overlap suggests a relationship between the speed of the coronal shock and the preferential propagation direction of the Moreton wave. The higher speed of the coronal shock in this direction can be attributed mainly to a special characteristic of the coronal medium and the magnetic field configuration through which the disturbance propagates, but the energy supplied initially by the piston driver could also account for this effect (Krause *et al.*, 2015). Figure 14 shows the Potential Field Source Surface (PFSS) model for Carrington rotation 2148 with the AR at central meridian passage (Figure 14a) and as viewed from the Earth on 29 March 2014 (Figure 14b). A region of open magnetic field lines can be seen

in correspondence with sectors 35 – 43, which sets favorable conditions for the propagation of a coronal MHD shock able to generate Moreton disturbances (Zhang *et al.*, 2011). Furthermore, the shock speed is fundamentally determined by the coronal magnetic field value, but the compression ratio decreases with increasing magnetic field (Krause *et al.*, 2015). Thus, the "field-line valley" to the north of AR 12017 with low magnetic field strength implies a region of high compression ratio, consequently a shock wave traveling through it can produce a strong compression over the chromosphere and eventually a Moreton signature. This is in agreement with the results found by Zhang *et al.* (2011), who analyzed the magnetic field configuration present in 13 Moreton events and concluded that the waves mostly propagate either in regions of large-scale closed magnetic loops or along valleys delimited by two sets of separated magnetic loops. Furthermore, given that close to the solar surface we expect a lower fast magneto-acoustic speed, the wavefronts will tend to curve downward, favoring compression over the chromosphere (Zhang *et al.*, 2011). All these facts support the hypothesis that the chromospheric Moreton fronts in our analyzed event are produced by a coronal shock wave.

A lobe comprising sectors 29 – 34 in which the wave speeds are high is shown in Figure 9. Following our previous discussion, these higher speed values cannot be attributed to a fast magneto-acoustic speed in the region since the magnetic field is low; this agrees with a high compression ratio. This speed asymmetry could be caused by the shock refracting in the high magnetosonic walls of the valley or by a particular behavior of a hypothetical piston producing the wave in this area (see Zhang *et al.*, 2011).

The non-radial propagation of the CME could be explained by the magnetic configuration to the north of AR 12017. The high magnetic pressure of the AR would force the CME ejection toward the north, where a lower magnetic pressure (because of the open field line region) would not impede the expansion and propagation of the magnetic structure sustaining the CME.

5.2. Correspondence between the Analyzed Regimes

The stack plots built from the angular sectors for Hα and He II (Figure 2) show a strong correlation both in time and surface distances, suggesting that they may respond to the same physical process. Nevertheless, the stack plots appear different when examined in detail, *i.e.* the Hα profiles exhibit brighter traces and the He II profiles show a discontinuous and granular appearance. For Hα, the seeing and other common ground-based perturbations strongly affect the data. In Hα, regions exhibiting double traces are noticeable (see features indicated by light blue arrows in sectors 36 – 39 of Figure 2a), suggesting the presence of more than a single coronal perturbation or a complex physical process that causes the differing chromospheric emissions. Other authors have suggested the presence of more than one Moreton wavefront in the vicinity of an AR (Muhr *et al.*, 2010; Francile *et al.*, 2013). However, in our case the spatial separation between these two fronts is not large enough to conclude about their presence on a firm basis. This double-trace effect is not visible in the He II stack plots.

Figure 8 shows AIA 193 Å DT maps with the superimposed splines traced from AIA 193 Å, Hα, and He II, all of them in the plane-of-sky frame, for six representative sectors. The black arrows in Figure 8 denote bright coronal features that appear to persist after the traces derived from Hα and He II data end. These features are located at coronal heights, but probably close to the solar surface. They could be caused by the shock front interacting with the lower denser layers of the corona, when the shock does not have enough speed or intensity to perturb the chromosphere. This suggests that disturbances like near-surface

EUV waves have the same physical origin as Moreton waves, *i.e.* compression in the low corona due to MHD waves or shocks. The low occurrence of Moreton events in relation to near-surface EUV waves can be attributed to large-amplitude EUV waves that are only weakly shocked or not shocked at all, and thus are not strong enough to disturb the much denser chromosphere, or to the particular characteristics of the coronal environment where they propagate.

The drifting of the center of the circumferences representing the shock-wave evolution (see Figures 9 and 10) inspires a model based on the intersection of a hypothetical spherical shock-front with the solar surface. Dome-shaped coronal waves with an almost circular appearance in EUV and soft X-ray observations have been reported by several authors (*e.g.* Vršnak *et al.*, 2002; Narukage *et al.*, 2004; Veronig *et al.*, 2010; Kozarev *et al.*, 2011; Ma *et al.*, 2011; Grechnev *et al.*, 2011b; Li *et al.*, 2012; Cheng *et al.*, 2012), while numerical simulations also confirmed this aspect (Warmuth, 2015, and references therein). If a common shock wavefront is responsible for all the effects, and if the model is accurate enough, then the intersection of a spherical shock-front with the solar sphere would coincide with the measured traces in the chromospheric and transition region, sector by sector. By combining the results derived from our measurements of the coronal-wave kinematics with the results found by other authors who analyzed the same event (see Section 4.3), the model is able to fit the coronal fronts to the chromospheric ones. The main difficulties of the model arise in the northwest and northeast directions. To the northwest of AR 12017 the model should fit the evolution of shock fronts moving away from the solar surface beyond the solar limb in the low corona, where the fast magneto-acoustic speed of the plasma constantly increases (Mann *et al.*, 1999); however, as shown in Figure 12a and 12b, the model (green line) stays below the chromospheric Hα and He II tracings (yellow and red lines, respectively). As mentioned in Section 5.1, the coronal shock-fronts bend toward the solar surface and have a dome shape (Warmuth, 2015), which implies that the measured distances [d_s] will not fit the model spheres, and therefore d_s to the west of the RP results in a shorter intersection distance with the chromosphere (see Figure 12a and 12b). The opposite is true to the east of the RP (see Figure 12e and 12f). This effect is also evident in Figure 9, where the westward shock fronts are closer together than those eastward. Some articles have reported that a lag between the coronal shock-front and the Hα chromospheric perturbation of $\approx$30 Mm is common (White, Balasubramaniam, and Cliver, 2014; Krause *et al.*, 2015). The misalignments in Figure 12 could be also partially attributed to this effect.

Figure 4b and 4c exhibit running-difference images in the AIA 193 Å and 211 Å bands, where an arc-like coronal feature denoted with green arrows can be seen. This feature propagates behind or jointly with the first shock front, depending on the sector. It is not possible to determine its full appearance or follow its propagation over a considerable period of time; however, we speculate that it may be related to the apparent dual traces visible in sectors 36 – 39 in the chromospheric DT-maps (Figure 2b).

In Section 4.4 we compared the slope and timings of the fastest AIA 193 Å wavefront with those of the shock ahead of the associated CME propagating in the LASCO C2 field of view. The good agreement evident from Figure 13 strongly suggests that the fastest EUV front corresponds to the white-light shock driven by the CME. The misalignment of the two sets of measurements from sector 29 (Figure 13a) may be due to the wave propagating with a large component away from the plane of view in this direction, while we used the plane-of-sky approximation to compare both data sets. The overall correspondence is in agreement with the unified picture of EUV waves synthesized from a series of findings by Patsourakos and Vourlidas (2012), whereby the inner brighter front is attributed to the expanding CME loops or bubble and the outer fainter front is the fast-mode wave ahead of the CME flanks

and leading edge. Further agreement is found with the findings by Kwon *et al.* (2013), who noted that the wavefront in the upper (white-light) solar corona is the counterpart of the EUV wave.

5.3. The Origin of the Shocks

We now discuss how the results of our modeling and of the wave-event analysis fit within the blast-wave and piston-driven shock scenarios, *i.e.* a flare-driven or CME-driven origin. As discussed above, the directional dependence of the speed can be explained by a spherical shock wavefront whose center moves mostly northward and outward from a RP. This suggests a piston-driven shock most likely produced by a CME moving in the direction of the model sphere center, in which the piston is directly behind the shock front and close to the upper sphere border. In this case, if they are visible in EUV, then the flanks of the piston should appear in the plane of vision as a circular-shaped feature within the ideal spherical shock. In this scenario, the apparent larger-speed lobe of sectors 29 – 34 could be an indication of the driver, distorted from the ideal shock sphere in the direction of its propagation.

The directional dependence of accelerations and speeds does not comply with the blast-wave scenario of shock generation in a fairly homogeneous coronal medium. This suggests either that the medium is not homogeneous or that the wave under study is not a blast-generated shock-wave. Although the region to the north of the AR appears to be homogeneous (see Figures 4 and 14), this is not the case in the vicinity of the AR, as is evident in Figure 9. In the case of a piston-driven shock, the shape of the shock wave is determined by the piston shape and the time elapsed until the piston stops acting as shock generator, as well as by the coronal medium.

In a flare-produced shock, a pressure pulse, static and close to the solar surface, would produce a shock of the blast-wave type. The constant speed of the sphere center used by our model cannot be in agreement with such a shock, even if it is considered that the shock evolves as a freely propagating blast wave after the piston stops acting as the wave driver.

The hypothesis of a flare impulsive pressure-pulse that generates a blast wave responsible for the Moreton event is also unlikely, given that the wave perturbation is seen to start in coincidence with the flare onset time [$t_{\rm on}$] (see Figure 7). It should be noted that the time $t_{\rm on}$ is determined from the same data taken as a basis for the DT maps. Following Vršnak and Cliver (2008), this coincidence cannot account for the necessary delay in the shock formation after the onset of the flare pressure pulse, given reasonable values of ambient Alfvén speed and piston expansion speed. Some authors have suggested that the launch of Moreton events precedes the flare impulsive phase (Veronig, Temmer, and Vršnak, 2008; Muhr *et al.*, 2010), while others find a close temporal coincidence (Warmuth *et al.*, 2004b; Temmer *et al.*, 2009; Francile *et al.*, 2013), thus indicating that probably not all Moreton events are similar in this sense.

To consider the hypothesis of piston-driven shock-wave generation, it is fundamental to understand the characteristics of the potentially associated piston. Kleint *et al.* (2015) measured the acceleration of the filament corresponding to this event, obtaining $3-5$ km s^{-2} between $t = 17{:}44{:}30$ UT and $t = 17{:}45{:}00$ UT, with the peak upflow velocity at $t = 17{:}45{:}40$ UT. In relation with another event, Temmer *et al.* (2009) found that a synthetic 3D piston of size ≈ 110 Mm accelerated to ≈ 4.8 km s^{-2} during ≈ 160 s, was able to generate a shock wave in correspondence with the Moreton-wave kinematics. Therefore, the fast ejection of the filament–CME ensemble can be regarded as the piston and thus as responsible for the shock wave generation. It is possible that after the flare impulsive phase this ensemble is not impulsively accelerated anymore, and therefore it continues evolving

with a nearly constant speed or decelerates, with the shock-wavefront persisting ahead of it. Otherwise, the filament–CME ensemble would not be able to generate a shock wave inside the AR, given the high magnetic field pressure of the region. Only when it reaches regions with lower magnetic pressure outside the AR, *i.e.* northwards, it is able to generate a shock wave that steepens and produces the chromospheric and coronal observable signatures (Vršnak and Cliver, 2008).

Although the model is not accurate enough to draw conclusive results, it yields a good approximation to the scenario of coronal wave generation. If the case of a shock generated by a temporary piston is true, then the 3D piston follows an approximate path given by $\boldsymbol{v} = (v_x, v_y, v_z)$, at least during the investigated time interval. The results of our model match well a sphere that expands at the speed of the fast-rising filament measured by Kleint *et al.* (2015) and Liu *et al.* (2015), suggesting an association between the filament eruption and the wave event. The piston could therefore be attributed to the front of the CME itself, or the full CME bubble or loops, as has been reported by several observational studies (Patsourakos and Vourlidas, 2012). Some observational reports reinforce this picture (Kienreich, Temmer, and Veronig, 2009; Patsourakos and Vourlidas, 2009; Veronig *et al.*, 2010; Grechnev *et al.*, 2011a). If this is the case, then the faster lobe of sectors 29 – 34 could be related to a piston provided by a CME structure, probably stretched, non-radially rising, *i.e.* with a northward inclination.

A CME evolving faster than the shock is not a coherent picture, given that the piston should generate and drive the shock. The circular feature indicated by green arrows in Figure 4 could therefore be attributed to a 3D rising structure bent to the north, *e.g.* an erupting CME bubble driving the shock ahead of it, whereas the observed outermost projected lateral extent of the shock (black arrows) maintains a circular shape.

By assuming that the piston decelerates and stops driving the shock wave at a certain point, as done by several authors (Patsourakos and Vourlidas, 2012, and references therein), the shock will become a freely propagating shock wave similar to a blast wave (Warmuth, 2015), but should prevail with the speed and shape imprinted by the driver at the initial stages. After some time, the shock front would tend to become more homogeneous and would depend on the particular conditions of the ambient corona and interplanetary space. The white-light observations give account of a CME and shock evolution following characteristics similar to those close to the origin.

5.4. Summary

We can summarize our main findings for the 29 March 2014 wave event as follows:

- The Moreton event exhibits the typical characteristics as regards speed, deceleration and angular span; nevertheless, the first Hα traces detected are at a relatively short distance from the brightest flare-kernel site, when compared with previous statistical results.
- The wave perturbation is seen to appear in coincidence with the estimated flare onset time.
- The analysis by sectors indicates a non-homogeneous angular behavior of the wavefronts in all analyzed wavelengths.
- Observations in He II 304 Å could be used as tracers and indicators of the existence of Hα Moreton waves even if the latter are not observed because of either unfavorable seeing conditions or a lack of ground-based data.
- The wave speed is higher in the northward direction, which cannot be attributed to a higher magnetic field strength since the field is open in that region. This higher speed could be related to the characteristics of the driver and region where the wave was ignited.

The lower magnetic field strength to the north of the AR favors compression over the chromosphere.

- Despite its simplicity, the proposed geometrical model is able to explain the measured chromospheric traces and the near-surface EUV wave signatures as the intersection of a spherically expanding shock-front with the chromosphere. This spherical shock can be explained as driven by a 3D piston that follows a northward and upward path. The shock trajectory and expansion speed are similar to those of the driver at its initial stages.
- The 3D piston can be attributed to the front of the CME or the full CME bubble, expanding at the speed of the associated rising filament.

We plan to apply our simple model to other Moreton events to test the generality of our results. If the model is found to be suitable, it could be applied to estimate the initial speeds and trajectories of ejected filaments or flux ropes during CME events.

Acknowledgements F.M. López, M.L. Luoni, H. Cremades, and C.H. Mandrini acknowledge financial support from grants PICT 2012-0973 (ANPCyT) and PIP 2012-01-403 (CONICET). C. Francile acknowledges support from grant PICTO 2009-0177 (FONCYT) and CICITCA-UNSJ E936. M.L. Luoni and C.H. Mandrini acknowledge the grant UBACyT 20020130100321. H. Cremades and F.M. López appreciate support from project UTI1744 (UTN). H. Cremades and C.H. Mandrini are members of the Carrera del Investigador Científico (CONICET). F.M. López is a fellow of CONICET. M.L. Luoni is a member of the Carrera del Personal de Apoyo (CONICET). D.M. Long is an Early Career Fellow funded by the Leverhulme Trust. We thank the referee of our manuscript for the constructive comments and suggestions.

Disclosure of Potential Conflicts of Interest The authors declare that they have no conflicts of interest.

References

Asai, A., Ishii, T.T., Isobe, H., Kitai, R., Ichimoto, K., UeNo, S.E.: 2012, *Astrophys. J. Lett.* **745**, L18. ADS. DOI.

Athay, R.G., Moreton, G.E.: 1961, *Astrophys. J.* **133**, 935. ADS. DOI.

Attrill, G., Harra, L., van Driel-Gesztelyi, L., Démoulin, P.: 2007, *Astrophys. J. Lett.* **656**, L101. ADS. DOI.

Attrill, G.D.R., Engell, A.J., Wills-Davey, M.J., Grigis, P., Testa, P.: 2009, *Astrophys. J.* **704**, 1296. ADS. DOI.

Bagalá, L.G., Bauer, O.H., Fernández Borda, R., Francile, C., Haerendel, G., Rieger, R.: 1999, In: Wilson, A., *et al.* (eds.) *Magnetic Fields and Solar Processes*, *ESA Special Publication* **448**, 469. ADS.

Balasubramaniam, K.S., Cliver, E.W., Pevtsov, A., Temmer, M., Henry, T.W., Hudson, H.S.: 2010, *Astrophys. J.* **723**, 587. ADS. DOI.

Benz, A.O.: 2008, *Living Rev. Solar Phys.* **5**, 1. ADS. DOI.

Brueckner, G.E., Howard, R.A., Koomen, M.J., Korendyke, C.M., Michels, D.J., Moses, J.D.: 1995, *Solar Phys.* **162**, 357. ADS. DOI.

Chen, P.F.: 2011, *Living Rev. Solar Phys.* **8**(1), 1. ADS. DOI.

Chen, P., Ding, M., Fang, C.: 2005, *Space Sci. Rev.* **121**(1–4), 201. ADS. DOI.

Chen, P.F., Fang, C.: 2005, In: Dere, K.P., Wang, J., Yan, Y. (eds.) *Coronal and Stellar Mass Ejections*, *Proceedings IAU Symposium* **226**, 55. ADS. DOI.

Chen, P., Fang, C., Shibata, K.: 2005, *Astrophys. J.* **622**(2), 1202. ADS. DOI.

Chen, P., Wu, Y.: 2011, *Astrophys. J. Lett.* **732**(2), L20. ADS. DOI.

Chen, P., Wu, T., Shibata, K., Fang, C.: 2002, *Astrophys. J. Lett.* **572**(1), L99. ADS. DOI.

Cheng, X., Zhang, J., Olmedo, O., Vourlidas, A., Ding, M.D., Liu, Y.: 2012, *Astrophys. J. Lett.* **745**, L5. ADS. DOI.

Cliver, E.W.: 2013, ISOON-based investigation of solar eruptions. Technical Report AFRL-RV-PS-TR-2014-0007, Air Force Research Laboratory.

Cremades, H., Iglesias, F.A., St. Cyr, O.C., Xie, H., Kaiser, M.L., Gopalswamy, N.: 2015, *Solar Phys.* **290**, 2455. ADS. DOI.

De Pontieu, B., Title, A.M., Lemen, J.R., Kushner, G.D., Akin, D.J., Allard, B.: 2014, *Solar Phys.* **289**, 2733. ADS. DOI.

Delaboudinière, J.-P., Artzner, G.E., Brunaud, J., Gabriel, A.H., Hochedez, J.F., Millier, F.: 1995, *Solar Phys.* **162**, 291. ADS. DOI.
Delannée, C.: 2000, *Astrophys. J.* **545**, 512. ADS. DOI.
Delannée, C., Aulanier, G.: 1999, *Solar Phys.* **190**(1–2), 107. ADS. DOI.
Delannée, C., Török, T., Aulanier, G., Hochedez, J.: 2008, *Solar Phys.* **247**(1), 123. ADS. DOI.
Fernandez Borda, R.A., Mininni, P.D., Mandrini, C.H., Gómez, D.O., Bauer, O.H., Rovira, M.G.: 2002, *Solar Phys.* **206**, 347. ADS. DOI.
Francile, C., Castro, J.I., Leuzzi, L., Luoni, M.L., Rovira, M., Cornudella, A.: 2008, *Bol. Asoc. Argent. Astron.* **51**, 339. ADS.
Francile, C., Costa, A., Luoni, M.L., Elaskar, S.: 2013, *Astron. Astrophys.* **552**(A3), 11. ADS. DOI.
Grechnev, V.V., Afanasyev, A.N., Uralov, A.M., Chertok, I.M., Eselevich, M.V., Eselevich, V.G.: 2011a, *Solar Phys.* **286**(2), 461. ADS. DOI.
Grechnev, V.V., Uralov, A.M., Chertok, I.M., Kuzmenko, I.V., Afanasyev, A.N., Meshalkina, N.S.: 2011b, *Solar Phys.* **273**, 433. ADS. DOI.
Halain, J.-P., Berghmans, D., Defise, J.-M., Renotte, E., Thibert, T., Mazy, E.: 2010 In: *Space Telescopes and Instrumentation 2010: Ultraviolet to Gamma Ray*, *Proc. SPIE* **7732**, 77320P. ADS. DOI.
Halain, J.-P., Berghmans, D., Seaton, D.B., Nicula, B., De Groof, A., Mierla, M.: 2013, *Solar Phys.* **286**, 67. ADS. DOI.
Hudson, H.S., Khan, J.I., Lemen, J.R., Nitta, N.V., Uchida, Y.: 2003, *Solar Phys.* **212**, 121. ADS. DOI.
Kaiser, M.L., Kucera, T.A., Davila, J.M., St. Cyr, O.C., Guhathakurta, M., Christian, E.: 2008, *Space Sci. Rev.* **136**, 5. ADS. DOI.
Khan, J.I., Aurass, H.: 2002, *Astron. Astrophys.* **383**, 1018. ADS. DOI.
Kienreich, I.W., Temmer, M., Veronig, A.M.: 2009, *Astrophys. J. Lett.* **703**, L118. ADS. DOI.
Kleint, L., Battaglia, M., Reardon, K., Sainz Dalda, A., Young, P.R., Krucker, S.: 2015, *Astrophys. J.* **806**, 9. ADS. DOI.
Kosugi, T., Matsuzaki, K., Sakao, T., Shimizu, T., Sone, Y., Tachikawa, S.: 2007, *Solar Phys.* **243**, 3. ADS. DOI.
Kozarev, K.A., Korreck, K.E., Lobzin, V.V., Weber, M.A., Schwadron, N.A.: 2011, *Astrophys. J. Lett.* **733**, L25. ADS. DOI.
Krause, G., Cécere, M., Francile, C., Costa, A., Elaskar, S., Schneiter, M.: 2015, *Mon. Not. Roy. Astron. Soc.* **453**(3), 2799. ADS. DOI.
Kwon, R.Y., Ofman, L., Olmedo, O., Kramar, M., Davila, J.M., Thompson, B.J., Cho, K.S.: 2013, *Astrophys. J.* **766**(55), 1. ADS. DOI.
Leenaarts, J., Carlsson, M., Rouppe van der Voort, L.: 2012, *Astrophys. J.* **749**, 136. ADS. DOI.
Lemen, J.R., Title, A.M., Akin, D.J., Boerner, P.F., Chou, C., Drake, J.F.: 2012, *Solar Phys.* **275**(1–2), 17. ADS. DOI.
Li, T., Zhang, J., Yang, S., Liu, W.: 2012, *Astrophys. J.* **746**, 13. ADS. DOI.
Lin, R.P., Dennis, B.R., Hurford, G.J., Smith, D.M., Zehnder, A., Harvey, P.R.: 2002, *Solar Phys.* **210**, 3. ADS. DOI.
Liu, W., Ofman, L.: 2014, *Solar Phys.* **289**, 3233. ADS. DOI.
Liu, W., Nitta, N.V., Schrijver, C.J., Title, A.M., Tarbell, T.D.: 2010, *Astrophys. J. Lett.* **723**, L53. ADS. DOI.
Liu, W., Ofman, L., Nitta, N.V., Aschwanden, M.J., Schrijver, C.J., Title, A.M., Tarbell, T.D.: 2012, *Astrophys. J.* **753**, 52. ADS. DOI.
Liu, C., Deng, N., Liu, R., Lee, J., Pariat, É., Wiegelmann, T.: 2015, *Astrophys. J. Lett.* **812**, L19. ADS. DOI.
Long, D.M., DeLuca, E.E., Gallagher, P.T.: 2011, *Astrophys. J. Lett.* **741**, L21. ADS. DOI.
Long, D.M., Gallagher, P.T., McAteer, R.T.J., Bloomfield, D.S.: 2011, *Astron. Astrophys.* **531**, A42. ADS. DOI.
Long, D.M., Bloomfield, D.S., Gallagher, P.T., Pérez-Suárez, D.: 2014, *Solar Phys.* **289**, 3279. ADS. DOI.
Ma, S., Raymond, J.C., Golub, L., Lin, J., Chen, H., Grigis, P.: 2011, *Astrophys. J.* **738**, 160. ADS. DOI.
Mann, G., Aurass, H., Klassen, A., Estel, C., Thompson, B.J.: 1999, In: Vial, J.-C., Kaldeich-Schü, B. (eds.) *8th SOHO Workshop: Plasma Dynamics and Diagnostics in the Solar Transition Region and Corona*, *ESA Special Publication* **446**, 477. ADS.
Markwardt, C.B.: 2009, In: Bohlender, D.A., Durand, D., Dowler, P. (eds.) *Astronomical Data Analysis Software and Systems XVIII*, *Astronomical Society of the Pacific Conference Series* **411**, 251. ADS.
Moreton, G.E.: 1960, *Astron. J.* **65**, 494. ADS. DOI.
Moreton, G.E., Ramsey, H.E.: 1960, *Publ. Astron. Soc. Pac.* **72**, 357. ADS. DOI.
Moses, D., Clette, F., Delaboudinière, J.-P., Artzner, G.E., Bougnet, M., Brunaud, J.: 1997, *Solar Phys.* **175**, 571. ADS. DOI.
Muhr, N., Vršnak, B., Temmer, M., Veronig, A.M., Magdalenić, J.: 2010, *Astrophys. J.* **708**, 1639. ADS. DOI.
Narukage, N., Hudson, H.S., Morimoto, T., Akiyama, S., Kitai, R., Kurokawa, H., Shibata, K.: 2002, *Astrophys. J. Lett.* **572**, L109. ADS. DOI.

Narukage, N., Morimoto, T., Kadota, M., Kitai, R., Kurokawa, H., Shibata, K.: 2004, *Publ. Astron. Soc. Japan* **56**, L5. ADS. DOI.
Narukage, N., Ishii, T.T., Nagata, S., UeNo, S., Kitai, R., Kurokawa, H.: 2008, *Astrophys. J. Lett.* **684**, L45. ADS. DOI.
Ontiveros, V., Vourlidas, A.: 2009, *Astrophys. J.* **693**, 267. ADS. DOI.
Patsourakos, S., Vourlidas, A.: 2009, *Astrophys. J. Lett.* **700**, L182. ADS. DOI.
Patsourakos, S., Vourlidas, A.: 2012, *Solar Phys.* **281**, 187. ADS. DOI.
Pesnell, W.D., Thompson, B.J., Chamberlin, P.C.: 2012, *Solar Phys.* **275**, 3. ADS. DOI.
Scherrer, P.H., Schou, J., Bush, R.I., Kosovichev, A.G., Bogart, R.S., Hoeksema, J.T.: 2012, *Solar Phys.* **275**, 207. ADS. DOI.
Seaton, D.B., Berghmans, D., Nicula, B., Halain, J.-P., De Groof, A., Thibert, T.: 2013, *Solar Phys.* **286**, 43. ADS. DOI.
Selwa, M., Poedts, S., DeVore, C.R.: 2012, *Astrophys. J. Lett.* **747**, L21. ADS. DOI.
Selwa, M., Poedts, S., DeVore, C.R.: 2013, *Solar Phys.* **284**, 515. ADS. DOI.
Temmer, M., Vršnak, B., Žic, T., Veronig, A.M.: 2009, *Astrophys. J.* **702**, 1343. ADS. DOI.
Thernisien, A., Vourlidas, A., Howard, R.A.: 2009, *Solar Phys.* **256**, 111. ADS. DOI.
Thompson, B.J., Plunkett, S.P., Gurman, J.B., Newmark, J.S., St. Cyr, O.C., Michels, D.J.: 1998, *Geophys. Res. Lett.* **25**, 2465. ADS. DOI.
Uchida, Y.: 1968, *Solar Phys.* **4**, 30. ADS. DOI.
Uchida, Y., Altschuler, M.D., Newkirk, G. Jr.: 1973, *Solar Phys.* **28**, 495. ADS. DOI.
Veronig, A.M., Temmer, M., Vršnak, B.: 2008, *Astrophys. J. Lett.* **681**, L113. ADS. DOI.
Veronig, A.M., Muhr, N., Kienreich, I.W., Temmer, M., Vršnak, B.: 2010, *Astrophys. J. Lett.* **716**, L57. ADS. DOI.
Vršnak, B., Cliver, E.W.: 2008, *Solar Phys.* **253**, 215. ADS. DOI.
Vršnak, B., Warmuth, A., Brajša, R., Hanslmeier, A.: 2002, *Astron. Astrophys.* **394**, 299. ADS. DOI.
Vršnak, B., Žic, T., Lulić, S., Temmer, M., Veronig, A.M.: 2016, *Solar Phys.* **291**, 89. ADS. DOI.
Warmuth, A.: 2010, *Adv. Space Res.* **45**, 527. ADS. DOI.
Warmuth, A.: 2015, *Living Rev. Solar Phys.* **12**, 3. ADS. DOI.
Warmuth, A., Mann, G.: 2011, *Astron. Astrophys.* **532**, A151. ADS. DOI.
Warmuth, A., Vršnak, B., Aurass, H., Hanslmeier, A.: 2001, *Astrophys. J. Lett.* **560**, L105. ADS. DOI.
Warmuth, A., Vršnak, B., Magdalenić, J., Hanslmeier, A., Otruba, W.: 2004a, *Astron. Astrophys.* **418**, 1101. ADS. DOI.
Warmuth, A., Vršnak, B., Magdalenić, J., Hanslmeier, A., Otruba, W.: 2004b, *Astron. Astrophys.* **418**, 1117. ADS. DOI.
Webb, D.F., Howard, T.A.: 2012, *Living Rev. Solar Phys.* **9**, 3. ADS. DOI.
White, S., Balasubramaniam, K., Cliver, E.: 2014, Direct Comparison of a solar Moreton wave, EUV wave and CME. Technical Report DTIC report AFRL-RV-PS-TP-2014-0004, Air Force Research Laboratory, Space Vehicles Directorate, 3550 Aberdeen Avenue SE, Kirtland AFB, NM 87117-5776.
Wuelser, J.-P., Lemen, J.R., Tarbell, T.D., Wolfson, C.J., Cannon, J.C., Carpenter, B.A.: 2004, In: Fineschi, S., Gummin, M.A. (eds.) *Telescopes and Instrumentation for Solar Astrophysics*, *Proc. SPIE* **5171**, 111. ADS. DOI.
Zhang, Y., Kitai, R., Narukage, N., Matsumoto, T., Ueno, S., Shibata, K., Wang, J.: 2011, *Publ. Astron. Soc. Japan* **63**, 685. ADS. DOI.